Plasmodium falciparum disruption of pericyte angiopoietin-1 secretion contributes to barrier breakdown in a 3D brain microvessel model

Rory K. M. Long[1,2], François Korbmacher[1], Paolo Ronchi[3], Hannah Fleckenstein[1,3], Martin Schorb[3], Waleed Mirza[1], Mireia Mallorquí[1], Ruth Aguilar[4], Gemma Moncunill[4], Yannick Schwab[3], Maria Bernabeu[1]*

[1]European Molecular Biology Laboratory (EMBL) Barcelona, Barcelona, Spain

[2]Heidelberg University, Faculty of Biosciences, Heidelberg, Germany

[3]European Molecular Biology Laboratory (EMBL), Cell Biology and Biophysics Unit, Heidelberg, Germany.

[4]Barcelona Institute for Global Health (ISGlobal), Hospital Clínic-Universitat de Barcelona, Barcelona, Spain

*To whom correspondence should be addressed. Email: maria.bernabeu@embl.es

Maria Bernabeu
EMBL Barcelona
Dr. Aiguader 88
Barcelona, Spain, 08003
maria.bernabeu@embl.es

The authors declare that they do not have any conflict of interest.

This work has been funded by the European Molecular Biology Laboratory (EMBL) and the European Research Council (ERC) , grant agreement no. 948088. F.K is funded through the Marie Skłodowska-Curie grant agreement (101068552). H.F is supported by a fellowship from the EMBL Interdisciplinary (EI4POD) program under Marie Skłodowska-Curie Actions COFUND (847543). G.M. is supported by RYC 2020–029886 I/ AEI/10.13039/501100011033, co funded by European Social Fund (ESF). ISGlobal received support from the grant CEX2018-000806-S funded by MCIN/AEI/ 10.13039/501100011033, and support from the Generalitat de Catalunya through the CERCA Program.

Abstract

Disruption of the vascular protective angiopoietin-Tie axis is common in cerebral malaria (CM) patients, with elevated angiopoietin-2 (Ang-2) and reduced angiopoietin-1 (Ang-1) blood concentrations. The role of pericytes in CM pathogenesis remains unexplored, despite being a major source of brain Ang-1 secretion and evidence of pericyte damage observed in CM postmortem samples. Here we engineered a 3D microfluidics-based microvessel model containing both human primary brain microvascular endothelial cells and pericytes. This model replicated pericyte vessel coverage and ultrastructural interactions present in the brain microvasculature. When exposed to *P. falciparum*-iRBC egress products, 3D brain microvessels presented decreased Ang-1 secretion, increased vascular permeability, and minor ultrastructural changes in pericyte morphology. Notably, *P. falciparum*-mediated barrier disruption was partially reversed after pre-treatment with recombinant Ang-1. Our approach suggests a novel mechanistic role of pericytes in CM pathogenesis and highlights the importance of the angiopoietin-Tie axis in vascular dysfunction caused by *P. falciparum*.

Introduction

Cerebral malaria (CM) is a severe neurological complication of *Plasmodium falciparum* infection, clinically characterized by coma and fatality rates averaging 15-20% [1]. Furthermore, approximately one third of CM survivors endure lifelong neurological sequelae such as hemiplegia, ataxia, epilepsy or speech disorders [2]. The majority of pediatric CM-related deaths present severe brain swelling due to vasogenic edema, likely as a consequence of blood-brain barrier dysfunction [3]. A hallmark of CM is the sequestration of *P. falciparum*-infected red blood cells (iRBC) in the brain microvasculature [4]. While the molecular players responsible for *P. falciparum*-iRBC ligand-receptor interactions with cerebral endothelial cells have been extensively studied [5–7], the consequences of iRBC sequestration to the brain microvasculature require further investigation. Nevertheless, evidence suggests that the increase in vascular permeability is a result of a multifaceted process including a blockade of barrier-supportive endothelial receptors by iRBC, the release of toxic *P. falciparum* products from egressed iRBC, and a dysregulated host innate immune response [8,9].

An important pathway commonly dysregulated in CM patients is the angiopoietin-Tie axis, crucial to maintaining endothelial pro-barrier, anti-inflammatory, and anti-apoptotic functions [10]. Binding of the vascular ligand angiopoietin-1 (Ang-1) to the endothelial receptor Tie-2 promotes vascular quiescence and the stabilization of endothelial tight junction proteins, such as Occludin and Zona Occludens-1 (ZO-1), necessary for maintaining the barrier function of the brain microvasculature [11–13]. Conversely, angiopoietin-2 (Ang-2), which is rapidly released from small endothelial storage granules called Weibel-Palade bodies, generally acts as a Tie-2 antagonist leading to endothelial activation and vascular leakage [14]. Given the opposing roles of these two molecules in vascular function, increased levels of Ang-2 and decreased levels of Ang-1 have been largely associated with cerebral vascular pathogenesis in a multitude of diseases [15,16]. Similarly, a decrease in Ang-1, and an increase in Ang-2 and the Ang-2:Ang-1 ratio has been well documented in fatal cases of both pediatric and adult CM [17–21]. Despite its importance, the mechanisms leading to angiopoietin-Tie axis disruption in CM are poorly understood. Human pro-inflammatory cytokines and pro-coagulation proteins, such as TNF-α and thrombin, have been proposed as responsible for the increase of Ang-2 secretion by endothelial cells [22,23], but the causative agent responsible for decreased secretion of Ang-1 in CM patients remains unknown.

Vascular mural cells, including smooth muscle cells and pericytes are the main cellular sources for Ang-1 secretion in the brain microvasculature [10]. Beyond Ang-1 secretion, pericytes support the microvasculature and promote quiescence through additional roles. Structurally, pericytes wrap

around cerebral microvessels and interact with the endothelium through reciprocal ultrastructural membrane protrusions, known as peg-and-socket junctions [24], and secrete extracellular matrix components of the microvascular basal lamina that strengthen microvascular architecture. Functionally, pericytes regulate brain blood flow by controlling vessel diameter through constriction [25]. Cerebral pericytes have been implicated in various vascular disorders of the central nervous system. Loss of pericytes from the cerebral vasculature in ischemic stroke and Alzheimer's disease is associated with blood-brain barrier disruption, extravasation of blood components into the brain parenchyma, and neuronal loss [26,27]. Similarly, histopathological studies in retinal samples of fatal pediatric CM cases have revealed pericyte damage in regions of *P. falciparum*-iRBC sequestration, suggesting a similar role of these cell types in severe malaria infections [28]. Yet, the role of cerebral pericytes in CM pathogenesis and in the dysregulation of the angiopoietin-Tie pathway remains largely unknown.

Bioengineered vascular models are emerging as powerful tools to study disease mechanisms *in vitro.* They have been successfully used to recapitulate many aspects of *in vivo* vascular disease including dysfunction of the angiopoietin-Tie pathway [29], and more recently, malaria pathogenesis, by modeling ligand-receptor interaction of iRBC in microvessels [30] or transcriptional changes on endothelial cells upon exposure to iRBC [31]. Here, we have further developed our existent 3D brain microvascular model [30], with the addition of pericytes to create a device that recapitulates *in vivo* interactions between both cell types. We have used this advanced model to understand the molecular basis of angiopoietin-Tie dysregulation in CM. Our results indicate that iRBC and products released during parasite blood stage egress play a role in angiopoietin-Tie dysregulation, and propose brain pericytes as a new player in CM pathogenesis.

Results

In vitro 3D brain microvessel model recapitulates *in vivo* cerebral endothelial-pericyte interactions

To investigate the role of cerebral pericytes in *P. falciparum*-mediated vascular pathogenesis, we have generated a 3D brain microvessel model that recapitulates the degree of pericyte coverage of the endothelium present in the brain microvasculature. The device is fabricated in a collagen type I hydrogel containing a microfluidic network with a pre-defined geometry, which is connected to both an inlet and outlet, enabling vessel perfusion [32]. Previous incorporation of pericytes in similar bioengineered 3D models involved cellular addition into the collagen hydrogel itself. However, this resulted in sparse interaction of pericytes with the endothelial microvessels [32]. Indeed, cerebral

120 pericytes have been shown to cover approximately one third of the brain microvasculature, albeit
121 with slight variations along the brain vascular hierarchical network [33,34]. In this model, primary
122 human brain vascular pericytes (HBVP) were seeded directly into the channels along with primary
123 human brain microvascular endothelial cells (HBMEC) at a 5:1 endothelial to pericyte ratio (Figure
124 1A). After 3 days in culture, the two cell types appear to reorganize into two different layers with
125 luminal endothelial cells and mCherry-expressing pericytes sitting on the 100 μm endothelial
126 channels (Figure 1B). Pericytes distributed homogenously around the vessel cross-section, with
127 approximately a third of the microvessel surface area covered by pericytes (29.6% of the bottom
128 surface and 27.3% of the top surface) (Figure 1C). Notably, endothelial VE-cadherin junctional
129 labeling is continuous along the vessel luminal surface, suggesting that the presence of pericytes
130 does not disrupt the endothelial layer (Figure 1D). Furthermore, endothelial cells in the microvessel
131 network express other common endothelial markers, such as von Willebrand factor, in addition to
132 adherens and tight junction markers, β-catenin and ZO-1 respectively (Figure 1E, Figure S1A,
133 Supporting information). Labeling by the mural cell marker, α-smooth muscle actin (αSMA), shows
134 that pericytes appear as elongated cells with thin processes stretching over multiple endothelial cells
135 (Figure 1D). Pericyte cellular identity was confirmed by the expression of a combination of cerebral
136 pericyte cellular markers including αSMA (Figure 1D), platelet derived growth factor receptor β
137 (PDGFRβ) and nerve/glial antigen 2 (NG-2) (Figure 1E, Figure S1B, Supporting information) [35,36].
138 PDGFRβ and NG-2 labeling of cerebral pericytes colocalized with laminin and collagen IV
139 staining, suggesting that pericytes contribute to the secretion of extracellular matrix components
140 that compose the basal lamina *in vivo* (Figure 1E) [37].

141

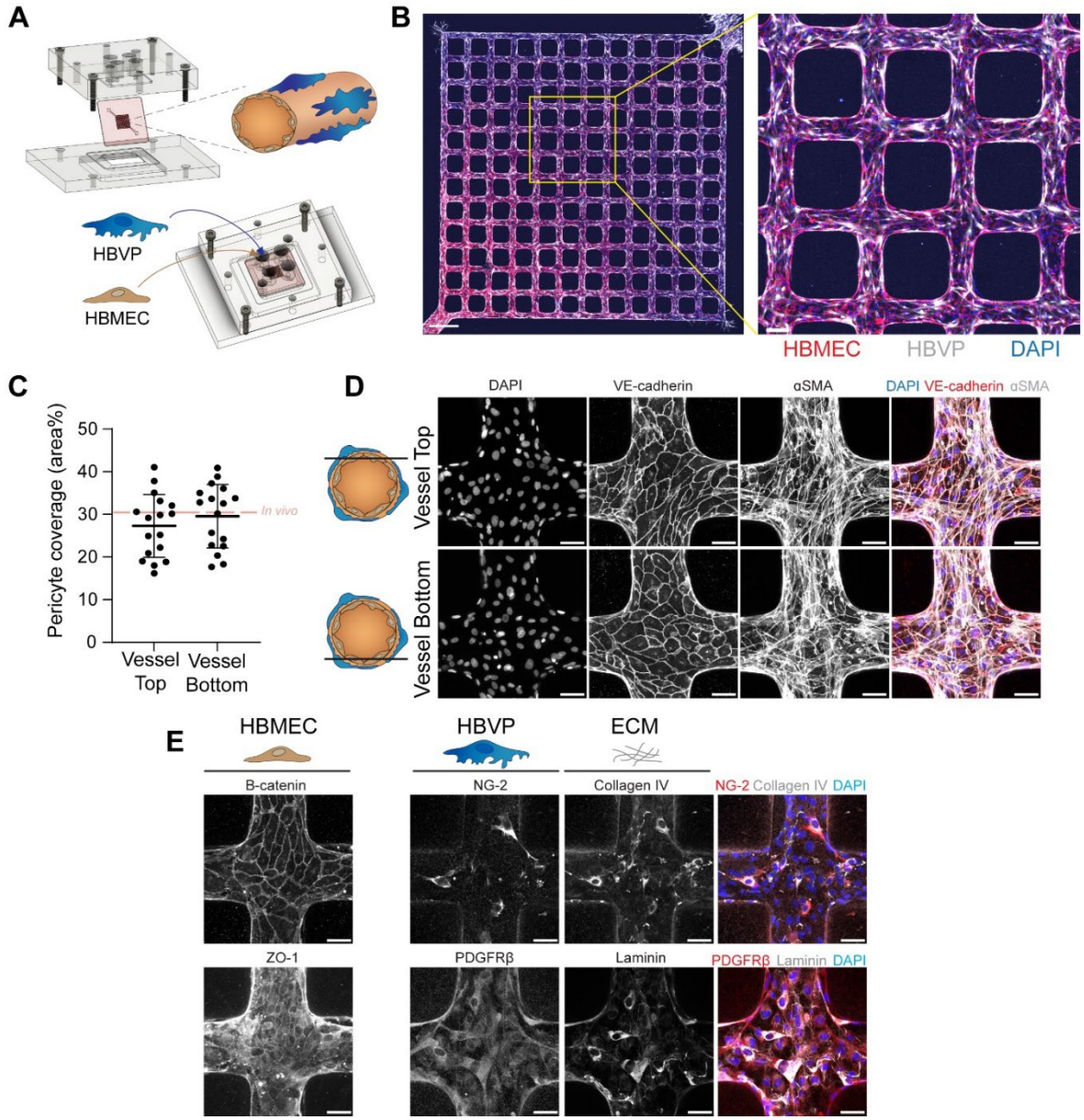

Figure 1. A) Schematic depiction of the fabrication pieces and device set-up (top-left), including a representation of resultant endothelial-pericyte interactions (top-right). Schematic depiction of the seeding method used to generate the 3D microvessel model (bottom). B) Immunofluorescence assay (IFA) maximum z-projection of the full network of cellularized channels labeled with Von-Willebrand factor for HBMEC (red), mCherry expressing HBVP (white) and DAPI (blue) (left). Inset highlighting pericyte coverage of the microvessels (right). Scale bars represent 500 µm and 100 µm (Inset). C) Quantification of the percentage of endothelial microvessel area covered by pericytes on either the top or bottom microvessel surface in a z cross-sectional view. Red dashed line represents estimated *in vivo* brain microvascular pericyte coverage. Data points represent quantification of 17 devices with statistical analysis determined by Mann-Whitney U test. Error bars represent mean +/- standard deviation. D) IFA maximum z-projection of VE-cadherin, αSMA, and DAPI labeling on the top and bottom cross-sectional surfaces of microvessels (left). Merge maximum z-projections with VE-cadherin (red), αSMA (white) and DAPI (blue) (right). E) IFA maximum z-projection of brain endothelial markers, ZO-1 and β-catenin, as well as, colocalization between brain pericyte markers, NG-2 and PDGFRβ (red), and extracellular matrix markers,

158 laminin and collagen IV (grey) in the presence of DAPI staining (blue). Scale bars represent 50 μm
159 in D and E.

160 Volumetric electron microscopy has been previously used to characterize *in vivo* 3D ultrastructural
161 interactions between pericytes and endothelial cells of the cerebral microvasculature [24]. To
162 characterize the spatial and ultrastructural organization of pericytes and endothelial cells in the
163 model, we utilized Serial Block-Face Scanning Electron Microscopy (SBF-SEM) [38], a volume
164 electron microscopy technique that provides nanoscale resolution of samples in a large field of view
165 [39]. We imaged a 100 μm segment of a microvessel branch with a 15x15x50 nm xyz resolution,
166 followed by cellular segmentation and rendering. We characterized microvessel coverage of
167 approximately 25 individual pericytes, distinguished from endothelial cells by the presence of a
168 highly granulated cytoplasm [40]. Cross-sectional analysis and segmentation of the microvessel
169 revealed an ovoid microvessel morphology, and confirmed the presence of pericytes at the
170 abluminal side of the endothelial cells (Figure 2A). Pericytes acquired a classical bump-on-a-log
171 morphology, with the soma being the thickest region of the cell, and their longitudinal axis aligned
172 with the direction of flow (Figure 2B). Most of the endothelial-pericyte interface is composed of
173 thin pericytic lamellae (100-300 nm thickness) that cover large areas of the endothelial surface,
174 with multiple thin pericytic branches appearing mostly at the cell periphery, as described previously
175 [24]. A close up of regions of pericyte-endothelial cell interaction reveal that the membranes of both
176 cell types are in close proximity, even though peg-and-socket junctions were not found (Figure 2C).
177 Pericytes constitute a heterogenous cell population depending on their location within the vascular
178 branch. Considering that our model possesses 100 μm diameter microvessels the co-expression of
179 αSMA, PDGFRβ and NG-2 staining, and the bump-on-a-log morphology(Figure 1D,E) is
180 reminiscent of ensheathing pericytes, commonly found on cerebral arterioles rather than capillary
181 pericytes that do not express αSMA [41,42]. Overall, the 3D *in vitro* brain microvessel model
182 recapitulates *in vivo* interactions between cerebral endothelial cells and pericytes, both at the tissue
183 and ultrastructural level, that can next be utilized to model the role of pericytes in malaria
184 pathogenesis.

185

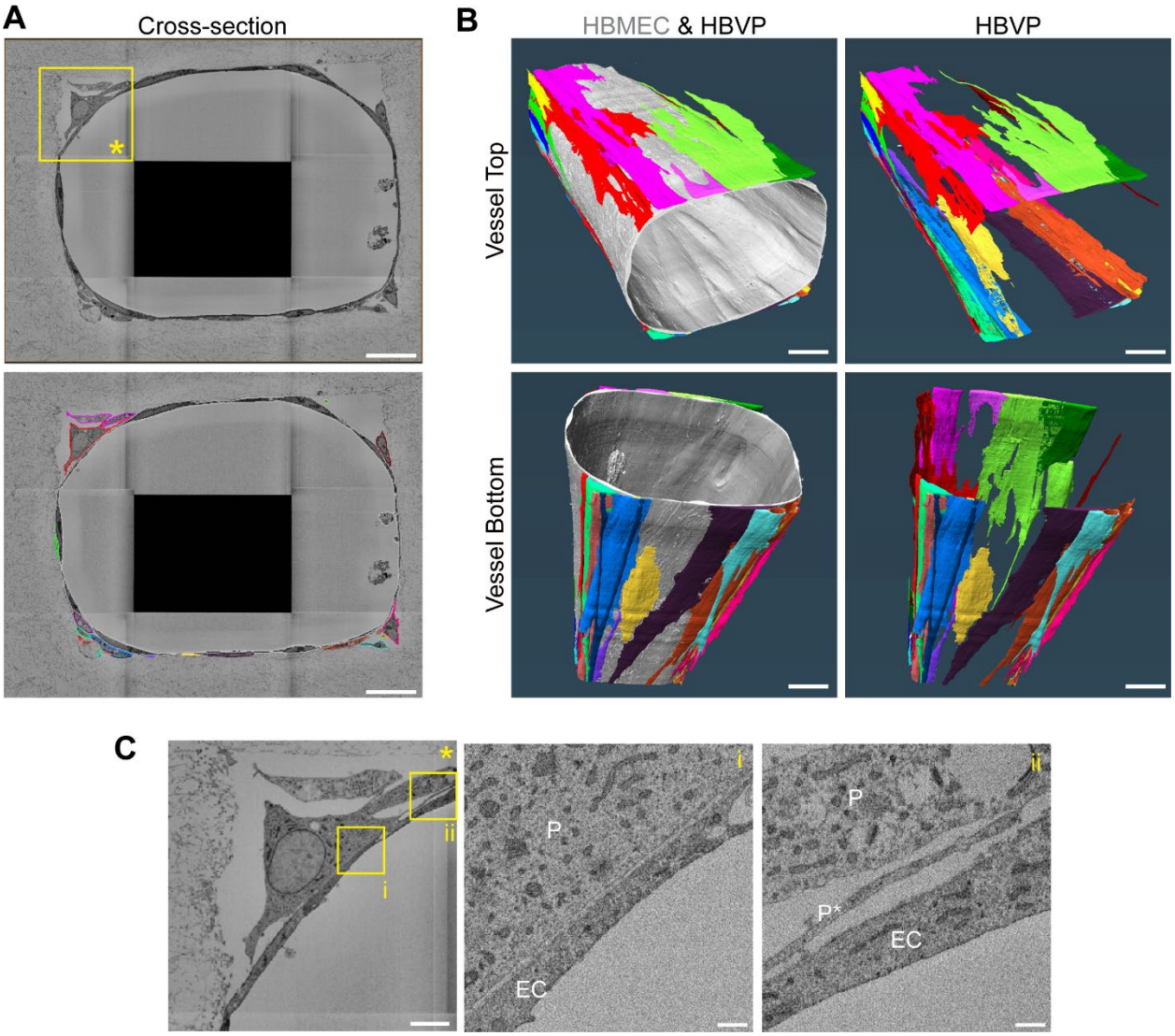

Figure 2. A) A cross-section of the microvessel imaged through the SBF-SEM volume (top) and the corresponding segmentation outlines of the endothelium (grey) and surrounding pericytes (coloured). Scale bars represent 20 µm. B) 3D rendering of the segmented microvessel (grey) and the surrounding pericytes viewed from above or below. Scale bars represent 10 µm. C) Zoomed images of the region of interest (ROI) in A. Insets show ROIs i and ii where pericytes are denoted with "P", endothelial cells by "EC" and pericyte lamellae by "P*". Scale bars represent 5 µm (left) and 500 nm in the insets (center and right).

196 ***P. falciparum* egress products increase vessel permeability but only cause minor changes in**
197 **pericyte morphology**

198 Multiple *in vitro* studies have shown that *P. falciparum* products released during malaria parasite
199 egress disrupt the endothelial barrier [43–47]. To characterize the impact that these could have on
200 pericyte function, we established a protocol to create media enriched for *P. falciparum*-iRBC
201 egressed products, denoted from here on as iRBC-egress media. Briefly, tightly synchronized
202 schizont stage-iRBCs were purified and allowed to egress in vascular growth media, followed by
203 recovery of the supernatant fraction containing *P. falciparum* soluble products at an estimated
204 concentration of $5x10^7$ ruptured iRBC/mL (equivalent to simultaneous egress of approximately a
205 1% parasitemia) (Figure S2A,B, Supporting information). We measured the endothelial disruptive
206 properties of iRBC-egress media by the xCELLigence system, which provides real time
207 measurement of cell barrier integrity through impedance. The *P. falciparum* egress products caused
208 a significant, dose-dependent decrease in cell index, a measurement of monolayer barrier function
209 normalized to untreated cells, that reached a maximum disruption at 18 hours (Figure S2C,
210 Supporting information). To elucidate if iRBC-egress media also induces barrier breakdown in the
211 brain 3D microvessel model, we performed permeability assays in a simpler microvessel network
212 which consists of a single 200 μm channel. After perfusion and incubation with iRBC-egress media
213 for 18 hours, *P. falciparum* egress products accumulated on the lateral and bottom walls of the
214 microvessel and appeared as dark spots in brightfield that were DAPI-positive by confocal
215 microscopy, suggesting the presence of hemozoin, food vacuoles and parasite DNA remnants
216 (Figure 3A,B). Microvessels perfused with iRBC-egress media presented a significant increase to
217 70 kDa FITC-dextran permeability across the entire vessel wall, corresponding to a 6-fold
218 increment compared to vessels perfused with vascular cell media ($4.08x10^{-6}$ cm/s in media-only vs.
219 $2.66x10^{-5}$ cm/s in devices exposed to iRBC-egress media) (Figure 3B,C).

220 To determine whether increased permeability was associated with physical changes in pericytes,
221 we assessed their cellular morphology in 3D microvessels exposed to iRBC-egress media for 18-
222 hours by SBF-SEM. Pericytes maintained close spatial proximity to the endothelium in the presence
223 of *P. falciparum*-iRBC ghosts, similar to control devices exposed to vascular growth media (Figure
224 3D). To investigate potential changes in pericyte shape, we isolated and analyzed each 3D rendered
225 pericyte (Figure 3E,F, Figure S3, Supporting information). Cellular features such as circularity and
226 maximum width did not differ between conditions, however, iRBC-egress media treated pericytes
227 presented fewer branches suggesting a response to iRBC-egress media (Figure 3E,F). Altogether,

our results show that *P. falciparum* egress products cause an increase in permeability of the 3D brain microvessel model, accompanied by minor changes in pericyte morphology.

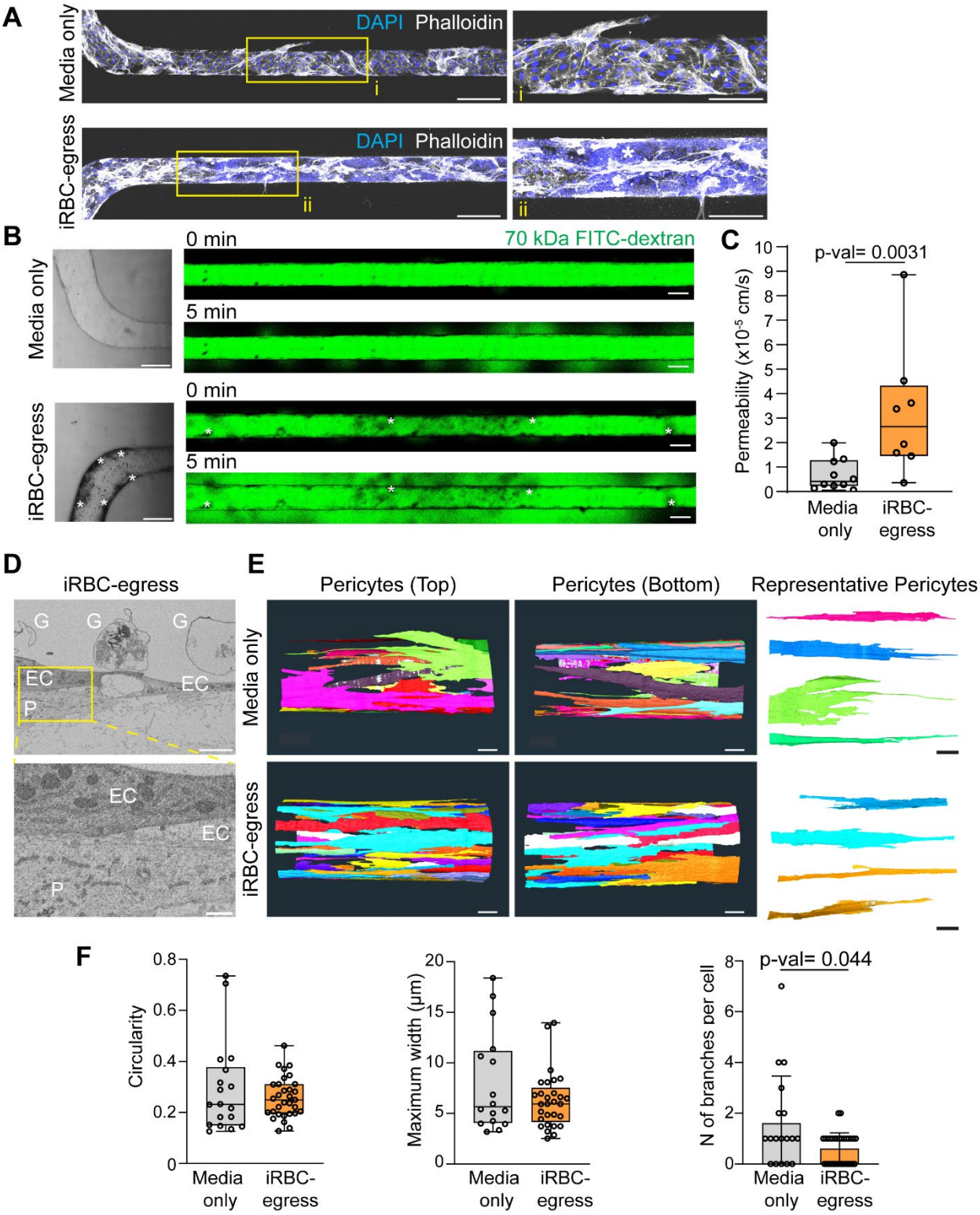

Figure 3. A) Fluorescence confocal imaging of phalloidin (white) and DAPI (blue) of single channel 3D brain microvessels treated with either media only or *P. falciparum*-iRBC-egress media for 18-hours. Insets show ROIs of i and ii that highlight endothelial junctions and pericyte coverage

(phalloidin). Accumulated DAPI-positive *P. falciparum*-iRBC egress material is denoted by an asterisk. Scale bars represent 200 µm (left) and 50 µm in inset (right). B) Brightfield images near the inlet of 3D brain microvessels after 18-hour incubation with media only or iRBC-egress media (left). Representative confocal images of 70 kDa FITC-dextran flux into the surrounding collagen 0 and 5 minutes after perfusion (right). Accumulated *P. falciparum*-iRBC egress material is represented with asterisks. Scale bars represents 200 µm. C) Apparent permeability of 70 kDa FITC-dextran in channels treated with media only or *P. falciparum*-iRBC egress media for 18-hours. Data points represent 8 individual devices. D) SBF-SEM image and zoomed ROI of microvessels treated with iRBC-egress media. Pericytes are denoted as "P", endothelial cells by "EC" and iRBC ghosts by "G". Scale bar represents 2 µm (top) and 500 nm in inset (bottom). E) 3D rendering of pericytes segmented from microvessels treated with media only or iRBC-egress media and imaged with SBF-SEM (left). Representative segmented pericytes for morphology analysis (right). Scale bar represents 10 µm. F) Circularity, maximum width and number (N) of branches analysis of 18 or 31 segmented pericytes treated with media only or iRBC-egress media respectively. Box and whisker plots display the median, 25th and 75th percentiles and the minimum and maximum data points, and statistical significance was measured by Mann-Whitney U test in both C and F.

***P. falciparum*-iRBCs induce dysregulation of the angiopoietin-Tie axis**

Next, we aimed to determine whether parasite egress products are a major driver of angiopoietin-Tie axis disruption characteristic of CM [17–20,48]. First, we determined through ELISA that pericytes are indeed the cell-type responsible for Ang-1 secretion, and not endothelial cells in a transwell model (Figure S4A, Supporting information). Then, we used a Luminex assay to measure secreted protein concentrations in microvessel supernatants recovered after 18-hour incubation with iRBC-egress media. Remarkably, we observed a substantial decline of Ang-1 secretion by pericytes, with concentrations (Figure 4A). Consistent with recent studies on 2D HBMEC monolayers [22], iRBC-egress media incubation did not result in increased Ang-2 secretion. Indeed, we quantified a significant decrease in Ang-2 secretion (Figure 4A). Despite Ang-2 decrease, a significant increase in the Ang-2:Ang-1 ratio was found (Figure 4*A*). Additionally, we observed a decrease in 3D microvessel secretion or shedding of other vascular factors important for endothelial-pericyte interaction, such as Neural cadherin (N-cadherin) and Tissue Inhibitor of Metalloproteinase-1 (TIMP-1) (Figure. S4A, Supporting information). Conversely, we detected no changes in Vascular Endothelial Growth Factor (VEGF), Tie-2, Angiopoietin-like-4 (ANGPTL4), Platelet Derived Growth Factor-BB (PDGF-BB), Interleukin-8 (IL-8) or Chemokine Ligand-1 (CXCL-1) after 18-hour incubation with iRBC-egress media (Figure S4A,B Supporting information).

To validate whether changes in the angiopoietin-Tie axis occur physiologically following *P. falciparum* blood stage egress within the microvasculature, we perfused the 3D brain microvessels with schizont stage *P. falciparum*-iRBC for 30 minutes followed by a 10-minute wash. After an 18-hour incubation period, supernatants were again recovered and analyzed by Luminex. Similar

results were obtained, with a reduction in both Ang-1 and Ang-2 secretion and an increase in the Ang-2:Ang-1 ratio (Figure 4B). Altogether, these results suggest that *P. falciparum*-iRBC hamper Ang-1 secretion by pericytes, revealing a previously unappreciated role of pericytes in the dysregulation of the angiopoietin-Tie axis in CM.

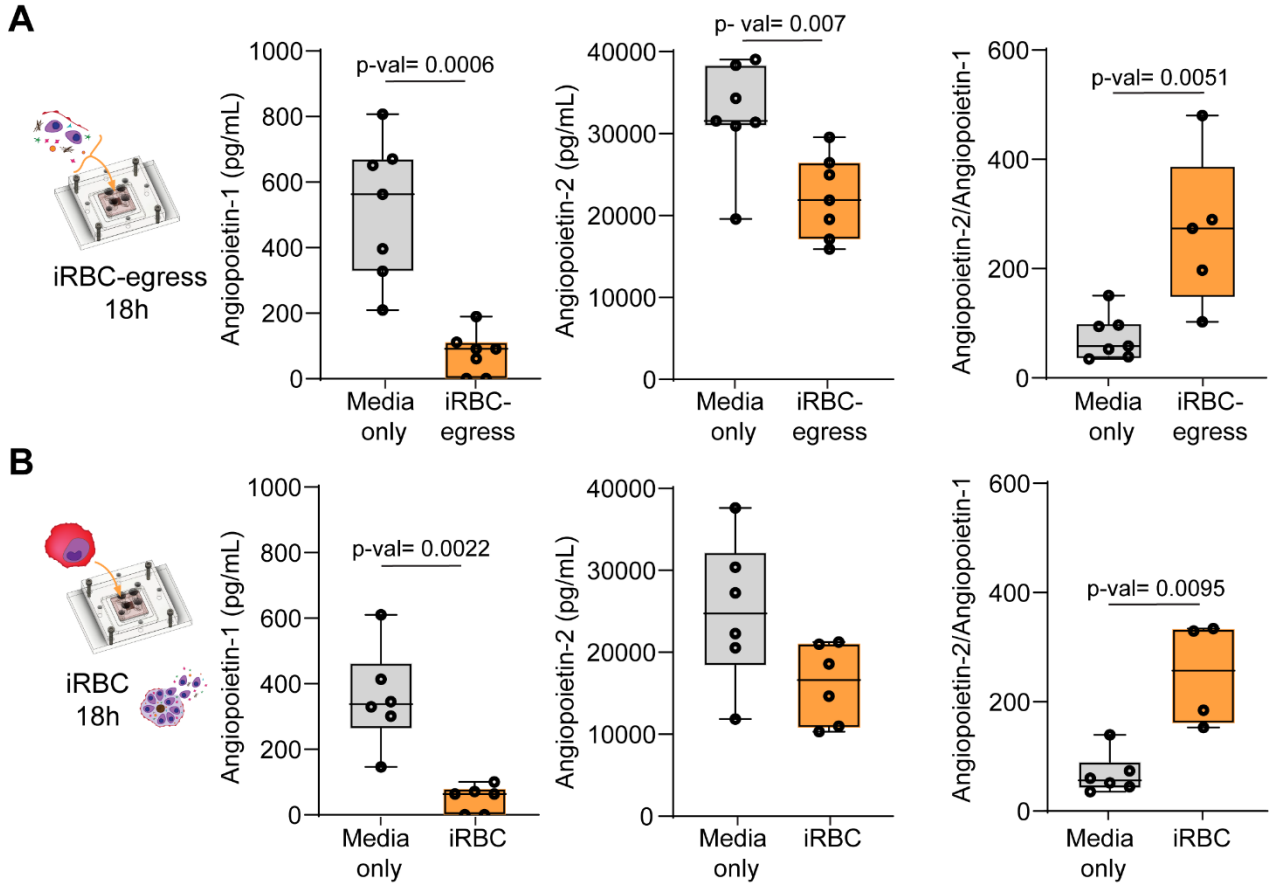

Figure 4. Ang-1 and Ang-2 concentrations measured from 3D brain microvessels treated with media only, iRBC-egress media A) or *P. falciparum*-iRBC B) for 18-hours (left and center). Ang-2:Ang-1 ratio in supernatants collected from 3D brain microvessels. Box and whisker plots display the median, 25th and 75th percentiles and the minimum and maximum data points. Data points represent supernatants pooled from 2-3 devices in 6-7 independent experiments and were analyzed by Mann-Whitney U test. Data points in which Ang-1 concentrations measured from 3D brain microvessels were below the limit of detection were removed to calculate the Ang-2:Ang-1 ratio.

287 **Recombinant Ang-1 partially protects against endothelial barrier breakdown by iRBC-egress**
288 **media**

289 Given the key role of Ang-1 to promote vascular quiescence and endothelial barrier formation we
290 investigated whether Ang-1 supplementation could protect against the barrier disruptive effects of
291 iRBC-egress media. First, we measured barrier disruption by xCELLigence in a 2D *in vitro*
292 endothelial culture in the absence of pericytes. An 18-hour pre-treatment of recombinant Ang-1
293 (rAng-1) to resting endothelium did not alter barrier properties. Conversely, an 18-hour pre-
294 treatment of rAng-1 prior endothelial cell exposure to iRBC-egress partially protected against
295 parasite-mediated endothelial barrier disruption (Figure 5A-C). While both iRBC-egress media
296 conditions follow parallel endothelial breakdown trajectories, rAng-1 addition dampened the
297 maximum levels of disruption by iRBC-egress media, and was followed by a faster recovery to
298 endothelial monolayer baseline levels (Figure 5B). Indeed, pre-treatment with rAng-1 conferred a
299 40% barrier breakdown protection after normalization to the untreated endothelial condition (Figure
300 5C). Nevertheless, shorter pre-treatment periods with rAng-1 (1-hour) did not protect against iRBC-
301 egress media disruption, suggesting that the establishment of endothelial protective pathways is not
302 immediate (Figure S5, Supporting information).
303 Next, we tested the protective capacity of rAng-1 against iRBC-egress products in the 3D
304 microvessel model (Figure 5D). While 3D microvessels presented a significant increase in
305 permeability values to 70 kDa FITC-dextran upon exposure to iRBC-egress media, a much smaller
306 non-significant increase was found when microvessels were pre-treated with rAng-1 for 18-hours
307 (Figure 5E,F). Indeed, Ang-1 pre-treatment presented a 45% protection when median permeability
308 values were compared (2.66×10^{-5} cm/s in iRBC-egress media vs. 1.45×10^{-5} cm/s iRBC-egress
309 media with rAng-1 pre-treatment), similar to that seen in 2D endothelial culture. Taken together,
310 pre-treatment with rAng-1 partially protects against microvascular permeability caused by *P.*
311 *falciparum* egress products, both in 2D and 3D, highlighting the importance that a decrease in Ang-
312 1 could have in CM pathogenesis.
313

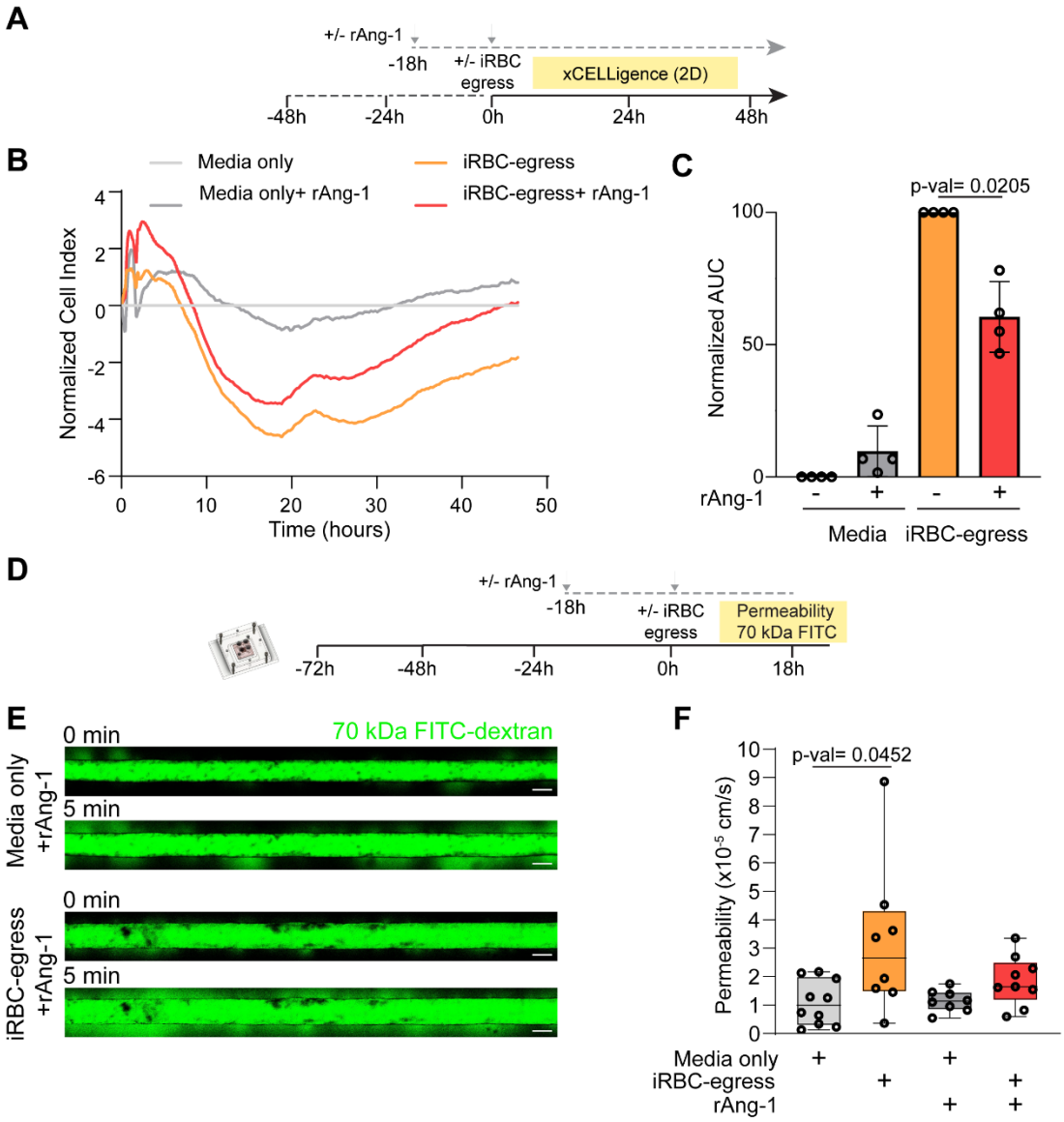

Figure 5. A) Experimental outline of the rAng-1 pre-treatment permeability experiment measured in 2D HBMEC monolayers in the absence of HBVP. B) Representative recording data of xCELLigence measurements taken after an 18-hour +/- rAng-1 pre-treatment followed by +/- iRBC-egress media addition. All conditions were normalized to the media only control. C) Area under the curve analysis of 4 independent experiments run in triplicate with iRBC-egress media normalized as 100. Error bars represent mean +/- standard deviation. Statistical significance is measured by repeated measures one-way ANOVA test with Dunnett's multiple comparisons test. D) Experimental outline of the rAng-1 pre-treatment permeability experiment on 3D brain microvessels. E) Confocal image of the 70 kDa FITC-dextran flux into the surrounding collagen at 0 and 5 minutes after dextran perfusion. Images correspond to a representative rAng-1 pretreated microvessel exposed to either media only or iRBC egress media for 18 hours. Scale bars represent 200 µm. F) Apparent permeability of 70 kDa FITC-dextran in microvessels pretreated with or without rAng-1 followed by 18-hour media only or iRBC egress media treatment in 8-10 individual devices per condition. Box and whisker plots display the median, 25th and 75th percentiles and the minimum and maximum data points. Statistical significance was analyzed by Kruskal-Wallis test with Dunn's multiple comparisons test.

Discussion

Disruption of the angiopoietin-Tie axis is a common feature in cerebral malaria patients, often associated with disease severity and fatality [18,20]. This dysregulation is also found in pediatric and adult severe malaria patients without cerebral complications [17,19] or in placental malaria [49]. Central to this pathway are cerebral pericytes, an Ang-1 secreting cell type that is located at the interface between the vasculature and brain parenchyma, yet largely understudied in the context of cerebral malaria. Here, we developed a 3D brain microvessel microfluidic model that recapitulates the high pericyte coverage present in the brain microvasculature. Exposure of the 3D brain microvessels to *P. falciparum*-egress products caused an increase in vascular permeability accompanied by a decrease in Ang-1. Furthermore, we showed that pre-treatment with rAng-1 could, at least, partially protect against endothelial barrier breakdown. Taken together, these results suggest that the cessation of Ang-1 release upon exposure to iRBC-egress products further contributes to microvessel disruption.

The bioengineered 3D model provides important vascular mechanical cues, including estimated flow and extracellular matrix stiffnesses present in the human brain. We could reproduce the high pericyte coverage found in brain capillaries by co-seeding primary cerebral endothelial cells and pericytes through the microfluidic network. Simultaneous cell seeding, at a ratio of 5:1 (endothelial cells: pericytes), did not prevent the formation of an intact luminal endothelial monolayer that presents continuous labeling of adherens and tight junctional markers. SBF-SEM microscopy showed that both cell types sit at nanoscale distance, with the presence of thin lamellae extending from the pericyte soma covering large areas of the endothelium. Yet, despite close proximity, the recently well-described reciprocal peg-and-socket junctions were absent in the model [24]. Overall, the 3D brain microvessel model recapitulates pericyte-endothelial interactions found in human brain vasculature making it suitable to study the role of pericytes in CM pathogenesis.

P. falciparum products released during blood stage egress have been shown to possess barrier breakdown capabilities on 2D endothelial monolayers grown on plastic. Proposed barrier disruptive *P. falciparum*-iRBC egress products include merozoite proteins, histones, heme, hemozoin and *P. falciparum* histidine rich protein 2 [22,43–47,50]. However, their effects on pericytes remain unexplored. In this study, we confirmed that these products are disruptive in a microfluidics-based 3D brain microvessel model in the presence of pericytes. Pericytes play an important role in maintaining vascular homeostasis. For example, loss of pericytes from the cerebral vasculature leads to increased permeability in mouse models [51]. Furthermore, dysregulation of cerebral pericytes and detachment from the vasculature have been observed in other cerebral vasculature

365 pathologies including stroke and Alzheimer's disease [26,27]. In our study, we did not observe gross
366 differences on pericyte morphology or loss of vascular coverage upon treatment with iRBC-egress
367 media. Nevertheless, pericytes from iRBC-egress media-treated 3D microvessels did display subtle
368 morphological changes, having significantly less branches. The relevance of these minor
369 ultrastructural modifications in vascular barrier dysfunction could imply molecular mechanisms of
370 disease. For example, Luminex quantification upon stimulation with iRBC-egress media in the 3D
371 brain microvessel model revealed a significant reduction in N-cadherin shedding. This could point
372 towards reduced functional endothelial-pericyte interaction upon short-term incubation with *P.*
373 *falciparum*-egress products. Future studies should explore whether exposure to *P. falciparum* for
374 longer timepoints recapitulates phenotypes observed in post-mortem samples of cerebral malaria
375 patients such as vacuolization [52] or pericyte loss [28]. Nevertheless, our results point towards a loss
376 of integrity at the endothelial and pericyte interface.

377 Ang-1 and Ang-2 have been considered in the past as potential biomarkers of cerebral malaria [53].
378 Ang-1 has excellent predictive power to distinguish malaria severity scores [19] or malaria from
379 other central nervous system febrile diseases [54]. Nevertheless, the underlying mechanism of Ang-
380 1 decrease in CM remains unknown, as previous *in vitro* studies overlooked the effect that iRBCs
381 could exert on brain pericytes. To our knowledge, our study is the first one to report that *P.*
382 *falciparum* products released upon iRBC egress halt Ang-1 secretion by pericytes. A
383 complementary hypothesis for Ang-1 decrease in CM patients could be that severe
384 thrombocytopenia, commonly associated with cerebral complications in *P. falciparum* infections
385 [7], plays an additional role as platelets are another major source of serum Ang-1 [55]. In light of this,
386 it is likely that both the effect of *P. falciparum*-iRBC on perivascular cells and thrombocytopenia
387 could work in concert to further contribute to a widespread decrease of Ang-1 levels. As for the
388 parasite component responsible for the cessation of Ang-1 secretion, the presence of accumulated
389 light scattering, DAPI-positive iRBC-egress material suggest a role of parasitic DNA or hemozoin,
390 yet further studies are necessary to identify which iRBC-egress derived component is responsible
391 for altered signaling pathways in pericytes. Nevertheless, our results highlight brain pericytes as a
392 new player in the development of CM through dysregulation in the secretion of Ang-1.

393 The use of recombinant Ang-1 as an adjunctive therapeutic against CM has long been of interest
394 [48] because of its role in strengthening endothelial tight junctions, as well as, upregulating anti-
395 apoptotic and anti-inflammatory pathways [56]. Interestingly, we showed that pre-incubation of
396 human microvessels with recombinant Ang-1 partially protected against iRBC-egress mediated
397 barrier breakdown. Nevertheless, the failure to achieve complete protection upon rAng1

398 supplementation hints at the existence of other pathogenic mechanisms involved in cerebral
399 malaria-induced barrier breakdown. While the concentration of recombinant Ang-1 utilized in this
400 study was supraphysiological compared to peripheral blood samples, it is quite likely that peripheral
401 blood concentrations underestimate local concentrations at the endothelial-pericyte interface. In our
402 model, protection was only achieved after a pre-incubation of 18-hours, suggesting that downstream
403 signaling through the Tie2 receptor, such as PI3K/Akt signaling, is required [10]. Future
404 interventions targeting the angiopoietin-Tie axis should focus on approaches that reverse
405 microvascular dysfunction after exposure to *P. falciparum.* As a proof of concept, recombinant
406 Ang-1 has previously been used as a treatment in a rodent experimental cerebral malaria model
407 after onset of disease, preserving blood-brain barrier integrity, and leading to a significantly
408 increased survival rate [48]. Although we did not observe complete protection after short term
409 exposure, our findings point towards a mechanistic role of Ang-1 in protecting against iRBC egress-
410 mediated endothelial barrier breakdown, further highlighting Ang-1 alteration as a functional
411 contributor to CM pathogenesis.

412 Clinical studies have shown a lack of correlation between Ang-2 levels and *P. falciparum*-iRBC
413 microvascular obstruction in the rectal microvasculature [57] or iRBC sequestration in brain post-
414 mortem samples [58]. Similarly, our study confirms that *P. falciparum*-iRBC sequestration in 3D
415 brain microvessel models does not directly cause Ang-2 secretion by endothelial cells. This result
416 is in concordance with a recent study that showed that Ang-2 is not secreted in response to *P.*
417 *falciparum* lysate products, but rather occurs following endothelial activation with TNF [22]. Other
418 studies have shown Ang-2 release as a result of exposure to thrombin or hypoxia [23,59], conditions
419 that have also been associated with CM pathogenesis. Altogether, our study is in agreement with
420 previous reports suggesting that *P. falciparum* sequestration does not play a direct role in the
421 secretion of Ang-2, which instead is more likely a consequence of the activation of host pro-
422 inflammatory factors.

423 To note, our study has several limitations, including the low-throughput of the model or challenges
424 in growing the devices for long periods of time, hence preventing the modelling of long-term
425 disruptive mechanisms, such as pericyte loss. Furthermore, our devices currently represent larger
426 microvessels of the brain given the 100 μm diameter of our model and α-SMA expression on
427 pericytes. Therefore, future studies could exploit 2-photon laser ablation or bioengineered self-
428 assembled models [60,61] to generate brain capillary-sized microvessels (5-10 μm), a major
429 pathogenic site in CM. Nevertheless, this study establishes a key role of pericytes on microvessels
430 that are similar in size to arterioles or post-capillary venules, regions of the brain vascular tree that

431 are equally damaged in CM patients [28]. Finally, an additional limitation of our model is the absence
432 of other cells that could play an important role in maintaining the angiopoietin-Tie axis. For
433 example, Ang-1 secretion has been described in other brain and blood cell types, such as smooth
434 muscle cells [62,63], platelets and more recently, neurons and astrocytes [64]. Yet, one of the major
435 advantages of *in vitro* bioengineered models is the opportunity to sequentially introduce different
436 components that, independently or collectively, could play a role in a complex and multifaceted
437 disease such as CM. In light of this, subsequent iterations of the model could introduce other cell
438 types that produce Ang-1 or incorporate pro-inflammatory cytokines or thrombin, to concurrently
439 model the functional consequence of increased secretion of Ang-2 by endothelial cells.

440 In summary, our study highlights the role that pericytes could have in the development of CM
441 pathogenesis by showing for the first time that egress of *P. falciparum*-iRBC interrupt Ang-1
442 secretion by pericytes. In addition, our findings confirm that external addition of Ang-1 partially
443 protects against the increase in vascular permeability mediated by *P. falciparum* egress products,
444 providing further evidence that interventions involving the angiopoietin-Tie axis could be part of a
445 multi-targeted adjunctive therapy against CM.

446

447 **Materials and Methods**

448 *Parasite lines:* HB3var03 variant *P. falciparum* parasites (dual ICAM-1 and EPCR binding),
449 regularly panned and monitored for appropriate PfEMP1 expression, were cultured in human B+
450 erythrocytes in RPMI 1640 medium (GIBCO) supplemented with 10% human type AB-positive
451 plasma, 5mM glucose, 0.4 mM hypoxantine, 26.8 mM sodium bicarbonate and 1.5 g/L gentamicin.
452 Parasites were grown in sealed top T75 flasks in a gas mixture of 90% N_2, 5% CO_2 and 1% O_2. To
453 maintain synchronous cultures, parasites were synchronized twice a week in their ring stage with
454 5% sorbitol and once a week in their trophozoite stage with 40 mg/mL gelaspan (Braun).

455 *P. falciparum-iRBC egress media preparation:* Late-stage *P. falciparum*-iRBC (schizonts,
456 parasitemia of 5-10%), synchronized in a 6-hour window, were purified by use of 40 mg/mL
457 gelaspan gradient separation to a final purity of >60% parasitemia. The enriched *P. falciparum*-
458 iRBC were then placed in complete RPMI media containing 1 μM compound 2, a reversible PKG
459 inhibitor that inhibits iRBC egress (kindly donated by Michael Blackman, The Francis Crick
460 Institute), at a concentration of 50 million *P. falciparum*-iRBC/mL. After 5 hours, compound 2
461 containing media was removed and the parasites were resuspended at a concentration of 100 million
462 *P. falciparum*-iRBC/mL in vascular growth media, put into a sealed top T25 flask, gassed and left

463 in the incubator overnight on a shaker set to 50 rpm to facilitate parasite egress. The resulting
464 parasite egress efficiency was assessed by a hemocytometer count and blood smear, and was then
465 concentrated to a working concentration of 50 million ruptured *P. falciparum*-iRBC/mL. The
466 resulting iRBC-egress media is spun at 1000 rpm to remove cellular debris and flash frozen in liquid
467 nitrogen until used. This concentration was chosen as this value is equivalent to a circulating
468 parasitemia of 1%, concentrations frequently found in malaria patients.

469 *Primary human brain microvascular endothelial cell and primary human brain vascular pericyte*
470 *culture:* Primary HBMEC (Cell Systems; ACBRI 376) were cultured according to the
471 manufacturer's recommendations in complete endothelial growth media-2MV (Lonza) containing
472 5% fetal bovine serum. Cells were split using Trypsin/EDTA. When 90% confluent, HBMEC were
473 seeded on 15 µg/mL Poly-L-lysine (P8920, Sigma) coated T75 flasks. Primary HBVP (ScienCell)
474 were cultured according to the manufacturer's recommendations in basal pericyte media
475 supplemented with 1% pericyte growth supplement, 1% penicillin/streptomycin and 2% fetal
476 bovine serum (ScienCell). Cells were split using Trypsin/EDTA when 90% confluent, seeded on
477 15 µg/mL Poly-L-lysine coated T75 flasks, and maintained in a humidified incubator at 37 °C and
478 5% CO_2. All experiments were conducted with HBMEC and HBVP with a passage number of 7-9.

479 *mCherry lentivirus transduction:* HBVPs were grown in a T75 flask to a ~90% confluency and
480 incubated with lentiviral particles containing a mCherry vector (kindly donated by Kristina Haase
481 Lab, EMBL Barcelona) in serum free pericyte media at a multiplicity of infection of 10. After 24
482 hours, the lentivirus particles were removed by washing once every 24-hours for a 2-day period.
483 mCherry-positive cells were then selected by fluorescence-activated cell sorting, expanded and
484 froze down for future experiments.

485 *3D brain microvessel model fabrication:* Type 1 collagen was extracted from rat tails, dissolved in
486 0.1% acetic acid, lyophilized in a freezer dryer (Labconco Freezone 2.5 Plus) and resuspended at
487 15 mg/mL in 0.1% acetic acid for storage. The stock collagen solution-0.1% acetic acid solution
488 was neutralized and diluted to 7.5 mg/mL on ice. A 13 by 13 channel grid or single channel pattern
489 were negatively imprinted into the collagen hydrogel by soft lithography using a PDMS stamp, and
490 inlet and outlets were created by insertion of stainless-steel dowel pins. The top pre-patterned
491 collagen hydrogel contained in a plexiglass top jig is sealed to a flat collagen-layered bottom that
492 sits on a coverslip and a plexiglass bottom jig. The assembly creates perfusable 120 µm diameter
493 microvessels (grid design) or 200 µm diameter microvessels (single channel design), as described
494 previously [32,65]. Prior to cell seeding, the channels were incubated with vascular growth media,
495 consisting in EGM-2MV (Lonza) supplemented with 1x pericyte and 1x astrocyte growth factors

496 (ScienCell) for 1 hour. Primary HBMECs and HBVPs, or mCherry-positive HBVPs (for pericyte
497 coverage analysis), were resuspended at concentrations of 7 million cells/mL and mixed to a ratio
498 of 5:1 HBMECs to HBVPs. The cell mixture was then seeded into the inlet in 8 μL increments and
499 driven through the microfluidic network by gravity-driven flow. Cells were perfused twice from
500 either the inlet or outlet until the channels were completely covered with adhered cells. Media was
501 then removed and devices were flipped upside down for 1-hour to ensure even cell distribution on
502 the top and bottom of the channels. Microvessels were cultured for 3 days before being used in
503 experiments with media change every twice per day by gravity driven flow.

504 *Immunofluorescence microscopy:* Microvessel labeling was performed by gravity driven flow.
505 Microvessels were fixed with 3.7% paraformaldehyde (PFA) in PBS for 15 minutes followed by
506 three 10-minute washes with PBS. Next microvessels were incubated with Background Buster
507 (Innovex) for 30 minutes and then permeabilized with blocking buffer (0.1% Triton X-100 and 2%
508 bovine serum albumin in phosphate-buffered saline (PBS)). Primary antibodies including rabbit
509 anti-αSMA-555 (EPR5368, Abcam), mouse anti-vWF (sc-365712, Santa Cruz), mouse anti-ZO-1
510 (Invitrogen, 10017242), rabbit anti-β-catenin (Cell Signaling, 9587S), mouse anti-PDGFRβ
511 (Abcam, ab69506), mouse anti-NG-2 (Invitrogen, 10424493), rabbit anti-laminin (Abcam,
512 ab11575), rabbit anti-collagen IV (Abcam, ab6586)), mouse anti-VE-cadherin (sc-52751, Santa
513 Cruz), and Phalloidin-647 (Invitrogen, A22287) were diluted in blocking buffer at 1:100 and
514 incubated overnight at 4 °C. After three 10-minute PBS washes, secondary antibodies including
515 goat anti-mouse Alexa Fluor 488 (A11001, Invitrogen), goat anti-rabbit Alexa Fluor 488
516 (Invitrogen, A-11008), goat anti-mouse Alexa Fluor 594 (Invitrogen, A-11005), goat anti-rabbit
517 Alexa Fluor 594 (Invitrogen, A-11012), goat anti-mouse Alexa Fluor 647 (A21235, Invitrogen),
518 goat anti-rabbit Alexa Fluor 647 (Invitrogen, A-21244) and 2 mg/mL DAPI (D21490, Invitrogen)
519 were diluted at 1:250 in 2% bovine serum albumin and 5% goat serum containing PBS, and
520 incubated at room temperature for 1 hour. Microvessels were washed 6 times with PBS for 10
521 minutes each and then imaged on a Zeiss LSM 980 Airyscan 2. Image stacks were acquired with 3
522 μm or 10 μm z-step size for single or tile scan images respectively. Z-projections and further
523 threshold analysis was done using Fiji (ImageJ v1.54f) software.

524 *Pericyte coverage analysis:* Tile scan images of the microvessel network with mCherry-positive
525 HBVP and vWF-labeled HBMEC were acquired as described above. Images were divided into two
526 stacks, one being the top half of the microvessels of the network and the other the bottom half.
527 Next, Z-projections of the top and bottom surfaces of the network were generated. The percentage

528 of endothelial surface that was covered by pericytes was calculated by creating a mask of both the
529 mCherry HBVP and the vWF-positive HBMEC.

530

531 *Serial Block-Face Scanning Electron Microscopy:* Microvessel devices were grown for 3 days,
532 then treated with iRBC-egress media or vascular growth media for 18hours, and then fixed by
533 adding 2% PFA and 2.5% glutaraldehyde (GA) to the device inlet for 30-minutes and washed twice
534 with EGM-2MV at 37 °C. The collagen hydrogel was then carefully removed from the plexiglass
535 jig and microvessel regions exposed to low shear stress were cut out and fixed with a secondary
536 fixative solution (2% PFA, 2.5% GA, 0.25 mM $CaCl_2$, 0.5 mM MgCl, 5% sucrose in a pH 7.4 0.1
537 M Cacodylate buffer) overnight at 4 °C, and then rinsed twice for 15-minutes with 0.1 M
538 Cacodylate buffer. Samples were post-fixed in a reduced Osmium solution (1% OsO_4, 1.5%
539 K_3FeCN_6 in 0.065 M Cacodylate buffer) for 2-hours at 4 °C followed by six 10-minute washes in
540 dH_2O. Post-staining consisted of subsequent incubation steps of 1% thiocarbohydrazide in dH_2O,
541 2% Osmium tetroxide in dH_2O, and 1% Uranyl acetate in dH_2O, aided by a PELCO Biowave Pro+
542 (Ted Pella) containing a SteadyTemp Pro and ColdSpot set to 20 °C at 7x 2 minute cycling on-off
543 at 100 W under vacuum, with dH_2O rinses in between steps once in a fume hood and twice in the
544 microwave at 250 W for 40 s without vacuum. The stained samples were then dehydrated by serial
545 additions of 30, 50, 80, and 100% ethanol solutions in the microwave at 250 W for 40 s without
546 vacuum with ColdSpot set to 4 °C, infiltrated with EPON 812 hard epoxy resin in steps of 25, 50,
547 75, 90, and 3x 100% resin diluted in ethanol with each step in the microwave at 150 W for 3 minutes
548 under vacuum and polymerized at 60 °C for 48 hours. The sample was trimmed (UC7, Leica
549 Microsystems) using a 90° cryo-trimmer (Diatome) to generate a small block face. The resulting
550 resin block was mounted on a pin stub using silver conductive epoxy resin (Ted Pella). The SBF-
551 SEM acquisition was performed with a Zeiss Gemini2 equipped with a Gatan 3view microtome
552 and a focal charge compensation device (Zeiss). The SEM was operated at 1.5 kV 300 pA, using a
553 pixel size of 15 nm, a slice thickness of 50 nm and a dwell time of 1.6 µs. The SBF-SEM acquisition
554 was performed using the software SBEMimage [66]. The acellular center of the lumen was not
555 imaged to save imaging time. Following acquisition, the positional metadata of the sections and
556 tiles obtained was converted with SBEM-specific import scripts
557 (https://git.embl.de/schorb/rendermodules-addons) for subsequent assembly, stitching and
558 alignment of large EM datasets [67]. Aligned images were then binned to 22 by 22 by 250 nm^3 in
559 xyz and segmentation was then performed using the software package Amira (Thermo Fischer
560 Scientific). Primary HBVP and HBMEC were segmented semi manually using the magic wand and

561 brush tool to segment every fifth section followed by use of the interpolation tool to segment the
562 entire volume. The resulting segmented microvessels were rendered using the generate surfaces
563 module for 3D visualization.

564 *P. falciparum-iRBC and iRBC-egress media perfusion to 3D brain microvessels:* All experiments
565 were done in 3D microvessel devices grown for 3 days. Schizont-stage *P. falciparum*-iRBC were
566 purified to >60% parasitemia by 40 mg/mL gelaspan and the resulting enriched population was
567 diluted in vascular growth media to 50 million iRBC/mL (same concentration as the *P. falciparum*-
568 iRBC-egress media). 200 µL of *P. falciparum*-iRBC or *P. falciparum*-iRBC-egress media was
569 added into the device inlet and perfused by gravity flow for 30-minutes with the outlet effluent
570 being reintroduced to the inlet every 10 minutes. Microvessels treated with intact *P. falciparum*-
571 iRBC (but not *P. falciparum*-iRBC-egress media), were then washed for 10 minutes with vascular
572 growth media. Both conditions were incubated overnight for 18 hours. Supernatant was then
573 removed from the outlet and pooled for Luminex analysis, and 3D brain microvessels were used
574 for permeability studies or fixed for imaging with 3.7% PFA for 15-minutes (see section
575 immunofluorescence microscopy).

576 *Fluorescent dextran-based permeability assay:* Single channel microvessel devices were grown for
577 3 days, then perfused and incubated for 18 hours with either vascular growth media or *P.*
578 *falciparum*-iRBC-egress media as described above. To determine resulting changes in
579 permeability, they were perfused with a 70 kDa FITC-dextran solution as follows: the device was
580 washed 1x with PBS and placed in a Zeiss LSM 980 Airyscan2 confocal microscope with a
581 temperature and CO_2 controlled imaging chamber (37 °C, 5% CO_2). PBS was aspirated and 100 µL
582 of 70 kDa FITC-dextran solution (100 µg/mL) in PBS was pulled from the inlet to the outlet at 6.5
583 µL/min flow rate using a syringe pump (Harvard Apparatus PHD 2000). Tilescan confocal images
584 of the entire channel were taken every 30 seconds for 5 minutes once the channel had been filled
585 with FITC dextran. In devices pre-treated with recombinant Ang-1 (923-AB-025, R&D Systems),
586 pre-incubation occurred at 18-hours, starting on day 2.

587 *Quantification of apparent permeability:* Apparent permeability is determined as the flux of
588 fluorescently labeled dextran across the microvessel wall into the surrounding collagen hydrogel.
589 All steps of permeability analysis were performed using ImageJ. By using the following equation:

590 $$Papp = \frac{1}{I_{Vt1} - I_{Tt1}} \times \frac{I_{Tt2} - I_{Tt1}}{\Delta t} \times \frac{A_{\text{lateral tissue}}}{P}$$

591 The apparent permeability (P_{app}) was calculated using the fluorescence intensity inside the vessel
592 (I_V) and in the surrounding collagen hydrogel (I_T) at two time points t1 (0 minutes after the vessel

is filled with dextran) and t2 (5 minutes after the vessel is filled). Δt is the change in time, $A_{lateral\ tissue}$ is the area of the collagen hydrogel being examined and P is the perimeter of the microvessel. To account for *P. falciparum*-iRBC-egress material that appears dark even in the presence of 70 kDa FITC-dextran, regions of *P. falciparum*-iRBC-egress material were excluded from the calculation of the fluorescence intensity inside the vessel (I_V) by using ImageJ median smoothing and the magic wand tool to select only the area of the channel without *P. falciparum*-iRBC-egress material.

Serial Block-Face Scanning Electron Microscopy pericyte morphology analysis: 3D-rendered pericyte meshes, segmented from SBF-SEM images of microvessels treated with either media alone or iRBC-egress media, were generated using Amira. Following segmentation, the meshes were exported as *STL* files and processed with a custom-developed Python script, designed to quantify aspects of pericyte morphology, including mesh circularity and maximum width [68]. Firstly, the 3D pericyte meshes were mapped onto a 2D plane through principal component analysis (PCA), effectively reducing the data's dimensionality while retaining its most significant morphological features. This mapping uses the two principal components that encapsulate the dimensions with the maximum variance in the 3D mesh, thus ensuring the conservation of structural information. Subsequently, convex hull analysis [69] was applied to delineate the pericyte mesh boundaries, providing a clear representation of each structure's shape by which circularity and maximum width could be measured. The circularity of each mesh is calculated using the convex hull, by assessing the ratio of the area enclosed by the hull to the square of the hull perimeter, with the formula for circularity given as $4\pi \times Area/Perimeter^2$. This circularity metric provides insight into the roundness of the mesh, where a value closer to 1 indicates a shape that is more circular, and values closer to 0 reflect more elongated or irregular shapes. Additionally, the maximum width is defined by identifying the two farthest points along the convex hull boundary and then calculating the greatest perpendicular distance from this line (connecting the farthest points) to any point within the convex hull. This measurement represents the maximum width of the pericyte mesh by assuming its length is the axis with the greater size. In addition, the number of pericyte branches was calculated manually by counting the number of branches on each 3D rendered pericyte.

Co-culture transwell fabrication: 10^5 HBVPs were seeded on the basolateral side of Poly-L-lysine treated transwell inserts (12 well PET membrane inserts with a pore size of 3 μm) in 100 μL of media and left to attach for 4-6 hours. Transwell inserts were then flipped into a 12 well culture plate containing 1200 μL of pericyte media and allowed to grow for 2 days. Next, 10^5 HBMECs were seeded onto the apical side of the Poly-L-lysine treated transwell inserts in 300 μL of media

626 and left to attach for 4-6 hours. Then media was removed from both sides of the insert and 1200 μL
627 of pericyte media was added to the basolateral side and 800 μL of EGM-2MV media to the apical
628 side. The cells were allowed to grow for 2 more days. On day 5, supernatants were taken from the
629 basolateral side for angiopoietin-1 ELISA. Endothelial cell-only transwells underwent the same
630 fabrication protocol minus the initial pericyte steps.

631 *Angiopoietin-1 ELISA:* Ang-1 protein concentrations were measured from supernatants taken from
632 the basolateral side of the transwell model. Supernatant concentrations were obtained by running
633 5X diluted samples on either the Human Angiopoietin-1 DuoSet ELISA kit (DY923, R&D
634 Systems). Protein concentrations were interpolated from sigmoidal 4-parameter-fit standard curves
635 generated from a 7-point standard curve of recombinant human proteins using GraphPad Prism.
636

637 *Quantification of secreted proteins by Luminex Assay:* Secreted protein concentrations were
638 measured from supernatants taken from the outlets of 3D brain microvessels with a 13 x 13 grid
639 geometry. Supernatants from 2-3 devices exposed to the same condition were pooled, diluted 2X
640 and assayed using a 10-plex Human Luminex Discovery Assay from R&D Systems on a Luminex
641 100/200. The 10-plex panel included: Ang-1, Ang-2, PDGF-BB, N-cadherin, TIMP-1, ANGPTL4,
642 VEGF, Tie-2, IL-8, and CXCL-1. Protein concentrations were interpolated from a 11-point standard
643 curve of known concentrations of recombinant human proteins provided by the vendor and reported
644 as pg/mL using xPONENT 4.2. 7 out of 10 analytes were in the standard curve quantification range
645 for 100% of measurements recorded, with Timp-1, N-cadherin and IL-8 having 100% of
646 measurements above the upper limit of quantification.

647 *Measuring changes in barrier integrity by xCELLigence:* 96 well PET E-plates (300600910,
648 Agilent) were coated with 15 μg/mL Poly-L-lysine and 5000 HBMECs in 200 μL EGM-2MV were
649 added per well. After cell adherence, the plate was placed into the xCELLigence RTCA SP reader
650 to begin baseline measurement of growth-related changes in cell index (an arbitrary measure of
651 impedance) and the cells were incubated for 3 days until cell index reached a plateau (indicative of
652 cell confluence). Media was changed every two days. For initial testing of the impact of iRBC-
653 egress media on barrier integrity, on the day of the experiment iRBC-egress media was added at
654 concentrations of either 12.5, 25 or 50 million ruptured iRBC/mL. Changes in cell index were
655 measured every 15-seconds for 8 hours and then every 15-minutes for 48-hours. To test the impact
656 of Ang-1 on *P. falciparum*-iRBC-egress media mediated barrier breakdown, iRBC-egress media
657 was added at $50x10^6$ ruptured iRBC/mL after either a 1- or 18-hour pre-incubation with 1 μg/mL
658 of rAng-1. Again, changes in cell index were measured every 15 seconds for 8 hours and then every

659 15-minutes for 48-hours. Quantification of partial protection was done by first normalizing each
660 condition to the media only control. Then the area under the curve of the negative values, indicative
661 of barrier breakdown, was calculated using GraphPad Prism (version 10.0.2) where the media only
662 without rAng-1 condition represented an average value of 0 and the iRBC-egress media without
663 rAng-1 condition an average value of 100.

664 *Statistical analysis:*All statistics were obtained by use of GraphPad Prism (version 10.0.2). Non-
665 parametric Mann-Whitney U tests were performed for most experiments, except to calculate Ang-
666 1 protection in the 2D xCELLigence and microvessel experiments in which a repeated measures
667 one-way ANOVA test with Dunnett's multiple comparisons test and Kruskal-Wallis test with
668 Dunn's multiple comparisons test were performed respectively. A P-value<0.05 was considered
669 statistically significant.

670 **Author contributions**

671 R.L and M.B conceived the work. R.L, P.R, R.A, and M.B designed experiments. R.L performed
672 most experiments with assistance of F.K, P.R, H.F, M.M, and R.A. R.L, P.R, H.F, W.M, R.A, Y.S,
673 G.M, M.B analyzed the data. R.L and M.B wrote the original draft of the manuscript. All authors
674 contributed to manuscript writing, revision, editing and suggestions.

675 **Acknowledgements**

676 We want to thank Kristina Haase (EMBL Barcelona) for her support and careful suggestions on the
677 project and manuscript writing, as well as for assistance with the generation of mCherry HBVP
678 with help from Violeta Beltran-Sastre. We acknowledge access to the CRG/UPF flow cytometry
679 facility for mCherry HBVP sorting. We are grateful to Carlota Dobaño (ISGlobal) for access to the
680 Luminex and to Michael Blackman (The Francis Crick Institute) who kindly gifted compound 2.
681 This work was facilitated by the EMBL Electron Microscopy Core Facility (EMCF), with important
682 assistance from Viola Oorschot on sample preparation and processing, and Karel Mocaer and
683 Martin Schorb on image analysis. The great majority of this work was supported by the core
684 program funding of the European Molecular Biology Laboratory (EMBL) and the European
685 Research Council (ERC) under the European Union's Horizon 2020 research and innovation
686 program (Grant agreement no. 948088). F.K is funded through the Marie Skłodowska-Curie grant
687 agreement (101068552). H.F is supported by a fellowship from the EMBL Interdisciplinary
688 (EI4POD) program under Marie Skłodowska-Curie Actions COFUND (847543). G.M. is supported
689 by RYC 2020–029886 I/ AEI/10.13039/501100011033, co funded by European Social Fund (ESF).

ISGlobal received support from the grant CEX2018-000806-S funded by MCIN/AEI/ 10.13039/501100011033, and support from the Generalitat de Catalunya through the CERCA Program. This research is part of the ISGlobal's Program on the Molecular Mechanisms of Malaria which is partially supported by the Fundación Ramón Areces.

Bibliography

[1] A. M. Dondorp, C. I. Fanello, I. C. Hendriksen, E. Gomes, A. Seni, K. D. Chhaganlal, K. Bojang, R. Olaosebikan, N. Anunobi, K. Maitland, E. Kivaya, T. Agbenyega, S. B. Nguah, J. Evans, S. Gesase, C. Kahabuka, G. Mtove, B. Nadjm, J. Deen, J. Mwanga-Amumpaire, M. Nansumba, C. Karema, N. Umulisa, A. Uwimana, O. A. Mokuolu, O. T. Adedoyin, W. B. Johnson, A. K. Tshefu, M. A. Onyamboko, T. Sakulthaew, W. P. Ngum, K. Silamut, K. Stepniewska, C. J. Woodrow, D. Bethell, B. Wills, M. Oneko, T. E. Peto, L. von Seidlein, N. P. Day, N. J. White, *The Lancet* **2010**, *376*, 1647.

[2] G. L. Birbeck, M. E. Molyneux, P. W. Kaplan, K. B. Seydel, Y. F. Chimalizeni, K. Kawaza, T. E. Taylor, *The Lancet Neurology* **2010**, *9*, 1173.

[3] S. Mohanty, L. A. Benjamin, M. Majhi, P. Panda, S. Kampondeni, P. K. Sahu, A. Mohanty, K. C. Mahanta, R. Pattnaik, R. R. Mohanty, S. Joshi, A. Mohanty, I. W. Turnbull, A. M. Dondorp, T. E. Taylor, S. C. Wassmer, *mSphere* **2017**, *2*, 10.1128/msphere.00193.

[4] K. Dorovini-Zis, K. Schmidt, H. Huynh, W. Fu, R. O. Whitten, D. Milner, S. Kamiza, M. Molyneux, T. E. Taylor, *The American Journal of Pathology* **2011**, *178*, 2146.

[5] A. Kessler, S. Dankwa, M. Bernabeu, V. Harawa, S. A. Danziger, F. Duffy, S. D. Kampondeni, M. J. Potchen, N. Dambrauskas, V. Vigdorovich, B. G. Oliver, S. E. Hochman, W. B. Mowrey, I. J. C. MacCormick, W. L. Mandala, S. J. Rogerson, D. N. Sather, J. D. Aitchison, T. E. Taylor, K. B. Seydel, J. D. Smith, K. Kim, *Cell Host & Microbe* **2017**, *22*, 601.

[6] J. Storm, J. S. Jespersen, K. B. Seydel, T. Szestak, M. Mbewe, N. V. Chisala, P. Phula, C. W. Wang, T. E. Taylor, C. A. Moxon, T. Lavstsen, A. G. Craig, *EMBO Molecular Medicine* **2019**, *11*, e9164.

[7] P. K. Sahu, F. J. Duffy, S. Dankwa, M. Vishnyakova, M. Majhi, L. Pirpamer, V. Vigdorovich, J. Bage, S. Maharana, W. Mandala, S. J. Rogerson, K. B. Seydel, T. E. Taylor, K. Kim, D. N. Sather, A. Mohanty, R. R. Mohanty, A. Mohanty, R. Pattnaik, J. D. Aitchison, A. Hoffmann, S. Mohanty, J. D. Smith, M. Bernabeu, S. C. Wassmer, *JCI Insight* **2022**, *6*.

[8] M. Bernabeu, J. D. Smith, *Trends in Parasitology* **2017**, *33*, 295.

[9] S. C. Wassmer, T. F. de Koning-Ward, G. E. R. Grau, S. Pai, *Trends in Parasitology* **2024**, *40*, 28.

[10] H. G. Augustin, G. Young Koh, G. Thurston, K. Alitalo, *Nat Rev Mol Cell Biol* **2009**, *10*, 165.

[11] S. Fukuhara, K. Sako, T. Minami, K. Noda, H. Z. Kim, T. Kodama, M. Shibuya, N. Takakura, G. Y. Koh, N. Mochizuki, *Nat Cell Biol* **2008**, *10*, 513.

[12] P. Saharinen, L. Eklund, J. Miettinen, R. Wirkkala, A. Anisimov, M. Winderlich, A. Nottebaum, D. Vestweber, U. Deutsch, G. Y. Koh, B. R. Olsen, K. Alitalo, *Nat Cell Biol* **2008**, *10*, 527.

[13] M. R. Siddiqui, C. S. Mayanil, K. S. Kim, T. Tomita, *PLOS ONE* **2015**, *10*, e0130857.

[14] P. C. Maisonpierre, C. Suri, P. F. Jones, S. Bartunkova, S. J. Wiegand, C. Radziejewski, D. Compton, J. McClain, T. H. Aldrich, N. Papadopoulos, T. J. Daly, S. Davis, T. N. Sato, G. D. Yancopoulos, *Science* **1997**, *277*, 55.

[15] S. Gurnik, K. Devraj, J. Macas, M. Yamaji, J. Starke, A. Scholz, K. Sommer, M. Di Tacchio, R. Vutukuri, H. Beck, M. Mittelbronn, C. Foerch, W. Pfeilschifter, S. Liebner, K. G. Peters, K. H. Plate, Y. Reiss, *Acta Neuropathol* **2016**, *131*, 753.

[16] J. Golledge, P. Clancy, J. Maguire, L. Lincz, S. Koblar, M. McEvoy, J. Attia, C. Levi, J. Sturm, O. P. Almeida, B. B. Yeap, L. Flicker, P. E. Norman, G. J. Hankey, *Stroke* **2014**, *45*, 1064.

[17] T. W. Yeo, D. A. Lampah, R. Gitawati, E. Tjitra, E. Kenangalem, K. Piera, R. N. Price, S. B. Duffull, D. S. Celermajer, N. M. Anstey, *Proceedings of the National Academy of Sciences* **2008**, *105*, 17097.

[18] F. E. Lovegrove, N. Tangpukdee, R. O. Opoka, E. I. Lafferty, N. Rajwans, M. Hawkes, S. Krudsood, S. Looareesuwan, C. C. John, W. C. Liles, K. C. Kain, *PLOS ONE* **2009**, *4*, e4912.

[19] A. L. Conroy, E. I. Lafferty, F. E. Lovegrove, S. Krudsood, N. Tangpukdee, W. C. Liles, K. C. Kain, *Malaria Journal* **2009**, *8*, 295.
[20] A. L. Conroy, S. J. Glover, M. Hawkes, L. K. Erdman, K. B. Seydel, T. E. Taylor, M. E. Molyneux, K. C. Kain, *Critical Care Medicine* **2012**, *40*, 952.
[21] V. Jain, N. W. Lucchi, N. O. Wilson, A. J. Blackstock, A. C. Nagpal, P. K. Joel, M. P. Singh, V. Udhayakumar, J. K. Stiles, N. Singh, *Malar J* **2011**, *10*, 383.
[22] C. Gomes, R. Varo, M. Duran-Frigola, A. Sitoe, R. Bila, S. Machevo, A. Mayor, Q. Bassat, A. Rodriguez, *JCI Insight* **2023**, *8*.
[23] U. Fiedler, M. Scharpfenecker, S. Koidl, A. Hegen, V. Grunow, J. M. Schmidt, W. Kriz, G. Thurston, H. G. Augustin, *Blood* **2004**, *103*, 4150.
[24] S. Ornelas, A.-A. Berthiaume, S. K. Bonney, V. Coelho-Santos, R. G. Underly, A. Kremer, C. J. Guérin, S. Lippens, A. Y. Shih, *J Cereb Blood Flow Metab* **2021**, *41*, 2185.
[25] R. Daneman, A. Prat, *Cold Spring Harb Perspect Biol* **2015**, *7*, a020412.
[26] F. Fernández-Klett, J. R. Potas, D. Hilpert, K. Blazej, J. Radke, J. Huck, O. Engel, W. Stenzel, G. Genové, J. Priller, *J Cereb Blood Flow Metab* **2013**, *33*, 428.
[27] J. D. Sengillo, E. A. Winkler, C. T. Walker, J. S. Sullivan, M. Johnson, B. V. Zlokovic, *Brain Pathology* **2013**, *23*, 303.
[28] V. Barrera, I. J. C. MacCormick, G. Czanner, P. S. Hiscott, V. A. White, A. G. Craig, N. A. V. Beare, L. H. Culshaw, Y. Zheng, S. C. Biddolph, D. A. Milner, S. Kamiza, M. E. Molyneux, T. E. Taylor, S. P. Harding, *eLife* **2018**, *7*, e32208.
[29] K. Haase, M. R. Gillrie, C. Hajal, R. D. Kamm, *Advanced Science* **2019**, *6*, 1900878.
[30] M. Bernabeu, C. Gunnarsson, M. Vishnyakova, C. C. Howard, R. J. Nagao, M. Avril, T. E. Taylor, K. B. Seydel, Y. Zheng, J. D. Smith, *mBio* **2019**, *10*, e00420.
[31] C. Howard, F. Joof, R. Hu, J. D. Smith, Y. Zheng, *Cell Reports* **2023**, *42*, 113253.
[32] Y. Zheng, J. Chen, M. Craven, N. W. Choi, S. Totorica, A. Diaz-Santana, P. Kermani, B. Hempstead, C. Fischbach-Teschl, J. A. López, A. D. Stroock, *Proceedings of the National Academy of Sciences* **2012**, *109*, 9342.
[33] T. M. Mathiisen, K. P. Lehre, N. C. Danbolt, O. P. Ottersen, *Glia* **2010**, *58*, 1094.
[34] M. T. Uemura, T. Maki, M. Ihara, V. M. Y. Lee, J. Q. Trojanowski, *Front. Aging Neurosci.* **2020**, *12*.
[35] L. He, M. Vanlandewijck, E. Raschperger, M. Andaloussi Mäe, B. Jung, T. Lebouvier, K. Ando, J. Hofmann, A. Keller, C. Betsholtz, *Sci Rep* **2016**, *6*, 35108.
[36] D. Attwell, A. Mishra, C. N. Hall, F. M. O'Farrell, T. Dalkara, *J Cereb Blood Flow Metab* **2016**, *36*, 451.
[37] F. Oliveira, O. Bondareva, J. R. Rodríguez-Aguilera, B. N. Sheikh, *Front. Cell. Neurosci.* **2023**, *17*.
[38] W. Denk, H. Horstmann, *PLOS Biology* **2004**, *2*, e329.
[39] C. J. Peddie, C. Genoud, A. Kreshuk, K. Meechan, K. D. Micheva, K. Narayan, C. Pape, R. G. Parton, N. L. Schieber, Y. Schwab, B. Titze, P. Verkade, A. Aubrey, L. M. Collinson, *Nat Rev Methods Primers* **2022**, *2*, 51.
[40] P. C. Nahirney, P. Reeson, C. E. Brown, *J Cereb Blood Flow Metab* **2016**, *36*, 413.
[41] L. C. D. Smyth, J. Rustenhoven, E. L. Scotter, P. Schweder, R. L. M. Faull, T. I. H. Park, M. Dragunow, *Journal of Chemical Neuroanatomy* **2018**, *92*, 48.
[42] R. I. Grant, D. A. Hartmann, R. G. Underly, A.-A. Berthiaume, N. R. Bhat, A. Y. Shih, *J Cereb Blood Flow Metab* **2019**, *39*, 411.
[43] M. R. Gillrie, G. Krishnegowda, K. Lee, A. G. Buret, S. M. Robbins, S. Looareesuwan, D. C. Gowda, M. Ho, *Blood* **2007**, *110*, 3426.
[44] J. Gallego-Delgado, U. Basu-Roy, M. Ty, M. Alique, C. Fernandez-Arias, A. Movila, P. Gomes, A. Weinstock, W. Xu, I. Edagha, S. C. Wassmer, T. Walther, M. Ruiz-Ortega, A. Rodriguez, *Journal of Clinical Investigation* **2016**, *126*, 4016.
[45] P. Pal, B. P. Daniels, A. Oskman, M. S. Diamond, R. S. Klein, D. E. Goldberg, *mBio* **2016**, *7*, 10.1128/mbio.00617.
[46] J. Storm, Y. Wu, J. Davies, C. A. Moxon, A. G. Craig, *Wellcome Open Res* **2020**, *5*, 34.

[47] C. A. Moxon, Y. Alhamdi, J. Storm, J. M. H. Toh, D. McGuinness, J. Y. Ko, G. Murphy, S. Lane, T. E. Taylor, K. B. Seydel, S. Kampondeni, M. Potchen, J. S. O'Donnell, N. O'Regan, G. Wang, G. García-Cardeña, M. Molyneux, A. G. Craig, S. T. Abrams, C.-H. Toh, *Blood Adv* **2020**, *4*, 2851.
[48] S. J. Higgins, L. A. Purcell, K. L. Silver, V. Tran, V. Crowley, M. Hawkes, A. L. Conroy, R. O. Opoka, J. G. Hay, S. E. Quaggin, G. Thurston, W. C. Liles, K. C. Kain, *Sci Transl Med* **2016**, *8*, 358ra128.
[49] V. Tran, A. M. Weckman, V. M. Crowley, L. S. Cahill, K. Zhong, A. Cabrera, R. E. Elphinstone, V. Pearce, M. Madanitsa, L. Kalilani-Phiri, V. Mwapasa, C. Khairallah, A. L. Conroy, F. O. ter Kuile, J. G. Sled, K. C. Kain, *eBioMedicine* **2021**, *73*.
[50] M. Zuniga, C. Gomes, Z. Chen, C. Martinez, J. C. Devlin, P. Loke, A. Rodriguez, *mBio* **2022**, *13*, e01746.
[51] A. Armulik, G. Genové, M. Mäe, M. H. Nisancioglu, E. Wallgard, C. Niaudet, L. He, J. Norlin, P. Lindblom, K. Strittmatter, B. R. Johansson, C. Betsholtz, *Nature* **2010**, *468*, 557.
[52] E. Pongponratn, G. D. H. Turner, N. P. J. Day, N. H. Phu, J. A. Simpson, K. Stepniewska, N. T. H. Mai, P. Viriyavejakul, S. Looareesuwan, T. T. Hien, D. J. P. Ferguson, N. J. White, *Am J Trop Med Hyg* **2003**, *69*, 345.
[53] G. M. de Jong, J. J. Slager, A. Verbon, J. J. van Hellemond, P. J. J. van Genderen, *Malaria Journal* **2016**, *15*, 581.
[54] A. L. Conroy, H. Phiri, M. Hawkes, S. Glover, M. Mallewa, K. B. Seydel, T. E. Taylor, M. E. Molyneux, K. C. Kain, *PLOS ONE* **2010**, *5*, e15291.
[55] R. L. Nachman, S. Rafii, *New England Journal of Medicine* **2008**, *359*, 1261.
[56] P. Saharinen, L. Eklund, K. Alitalo, *Nat Rev Drug Discov* **2017**, *16*, 635.
[57] J. Hanson, S. J. Lee, M. A. Hossain, N. M. Anstey, P. Charunwatthana, R. J. Maude, H. W. F. Kingston, S. K. Mishra, S. Mohanty, K. Plewes, K. Piera, M. U. Hassan, A. Ghose, M. A. Faiz, N. J. White, N. P. J. Day, A. M. Dondorp, *BMC Medicine* **2015**, *13*, 122.
[58] P. Prapansilp, I. Medana, N. T. H. Mai, N. P. Day, N. H. Phu, T. W. Yeo, T. T. Hien, N. J. White, N. M. Anstey, G. D. Turner, *Malaria Journal* **2013**, *12*, 50.
[59] P. Pichiule, J. C. Chavez, J. C. LaManna, *Journal of Biological Chemistry* **2004**, *279*, 12171.
[60] C. Arakawa, C. Gunnarsson, C. Howard, M. Bernabeu, K. Phong, E. Yang, C. A. DeForest, J. D. Smith, Y. Zheng, *Sci. Adv.* **2020**, *6*, eaay7243.
[61] C. Hajal, G. S. Offeddu, Y. Shin, S. Zhang, O. Morozova, D. Hickman, C. G. Knutson, R. D. Kamm, *Nat Protoc* **2022**, *17*, 95.
[62] C. Sundberg, M. Kowanetz, L. F. Brown, M. Detmar, H. F. Dvorak, *Laboratory Investigation* **2002**, *82*, 387.
[63] T. Nishishita, P. C. Lin, *Journal of Cellular Biochemistry* **2004**, *91*, 584.
[64] X. Wei, S. Jessa, C. L. Kleinman, T. N. Phoenix, *Developmental Neuroscience* **2021**, *43*, 321.
[65] L. Piatti, C. C. Howard, Y. Zheng, M. Bernabeu, In *Malaria Immunology* (Eds.: Jensen, A. T. R.; Hviid, L.), Springer US, New York, NY, **2022**, pp. 557–585.
[66] B. Titze, C. Genoud, R. W. Friedrich, *Front. Neural Circuits* **2018**, *12*.
[67] G. Mahalingam, R. Torres, D. Kapner, E. T. Trautman, T. Fliss, S. Seshamani, E. Perlman, R. Young, S. Kinn, J. Buchanan, M. M. Takeno, W. Yin, D. J. Bumbarger, R. P. Gwinn, J. Nyhus, E. Lein, S. J. Smith, R. C. Reid, K. A. Khairy, S. Saalfeld, F. Collman, N. Macarico da Costa, *eLife* **2022**, *11*, e76534.
[68] waleedmirzaPhD, *waleedmirzaPhD/cell_analysis_toolkit*, **2024**.
[69] P. Virtanen, R. Gommers, T. E. Oliphant, M. Haberland, T. Reddy, D. Cournapeau, E. Burovski, P. Peterson, W. Weckesser, J. Bright, S. J. van der Walt, M. Brett, J. Wilson, K. J. Millman, N. Mayorov, A. R. J. Nelson, E. Jones, R. Kern, E. Larson, C. J. Carey, İ. Polat, Y. Feng, E. W. Moore, J. VanderPlas, D. Laxalde, J. Perktold, R. Cimrman, I. Henriksen, E. A. Quintero, C. R. Harris, A. M. Archibald, A. H. Ribeiro, F. Pedregosa, P. van Mulbregt, *Nat Methods* **2020**, *17*, 261.

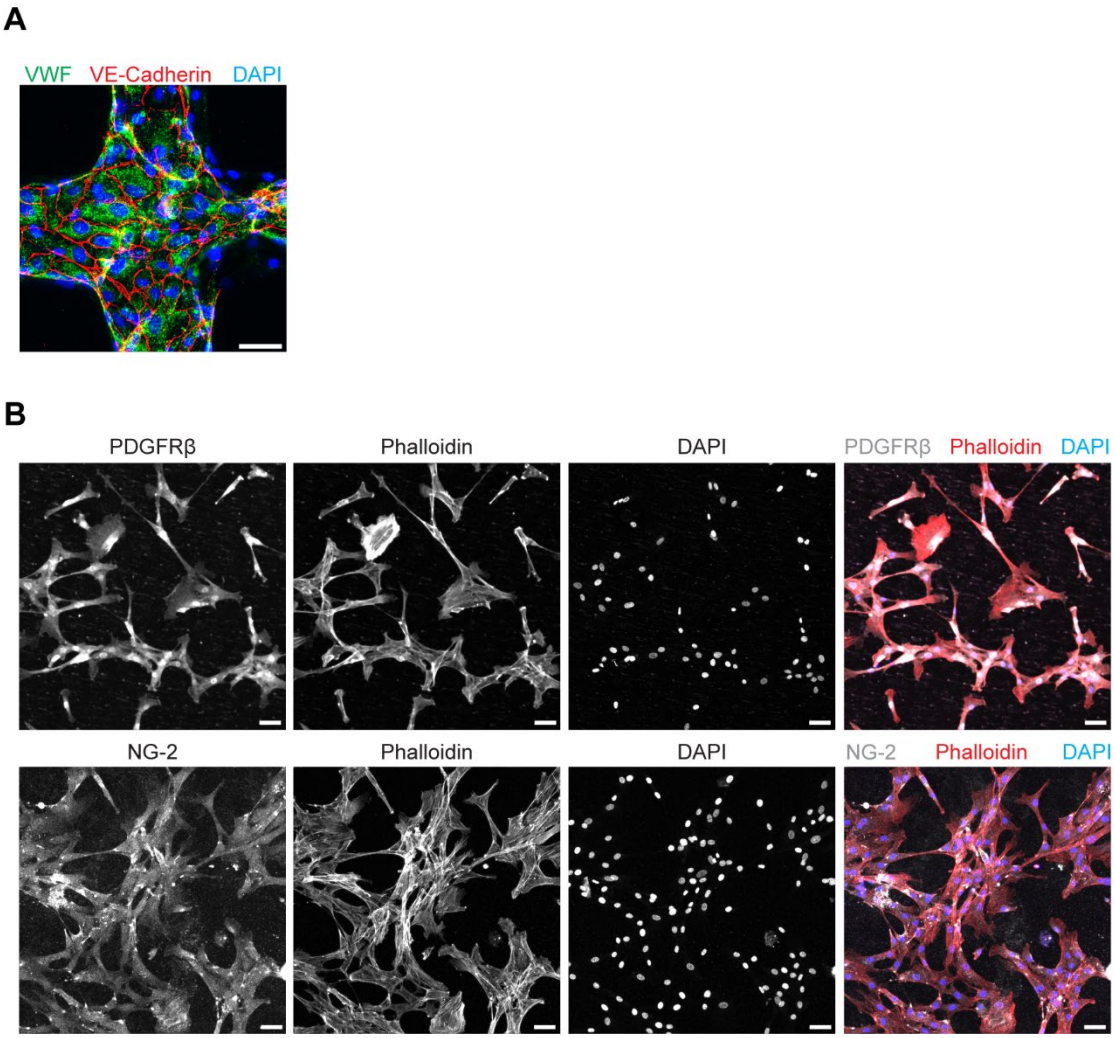

Figure S1. A) Immunofluorescence maximum z-projection of von Willebrand factor (VWF, green), VE-cadherin (red) and DAPI (blue) labeling on 3D microvessel channel B) PDGFRβ (top) and NG-2 (bottom) staining. Cell cytoskeleton is labelled with Phalloidin in 2D HBVP monolayers. The merge staining includes the pericyte markers (white), phalloidin (red) and DAPI DAPI labeling (blue). Scale bar represents 50 µm in A and B.

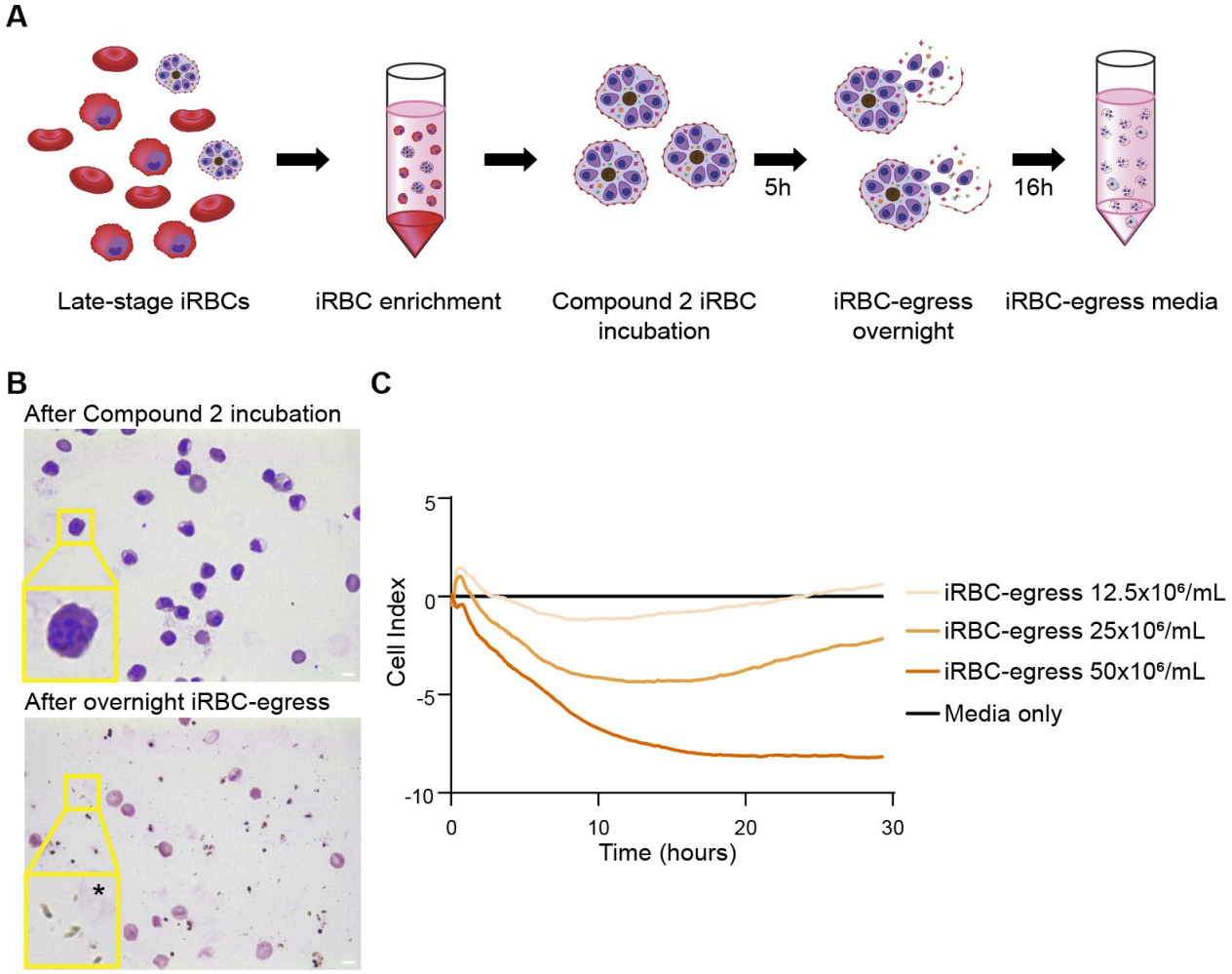

Figure S2. A) Schematic representation of the protocol to make iRBC-egress media. In short, late-stage *P. falciparum*-iRBC are purified by a gelaspan gradient separation and then incubated for 5 hours with compound-2 to synchronize them at the point of egress. Compound-2 is removed and the *P. falciparum*-iRBC are resuspended in vascular growth media and left overnight on a shaker at 50 rpm to egress. B) A thin smear of tightly synchronized schizonts before the removal of Compound-2 (yellow inset highlights a ROI with a schizont-stage iRBC) or the resultant iRBC-egress media before centrifugation (yellow inset highlights a ROI with free hemazoin particles next to an iRBC ghost, denoted with an asterisk) stained with giemsa. Scale bar represents 5 µm. **C**) Representative recording data of xCELLigence measurements on 2D HBMEC monolayers in the absence of HBVP taken after addition of iRBC-egress media at different concentrations. Data is normalized to the media-only control.

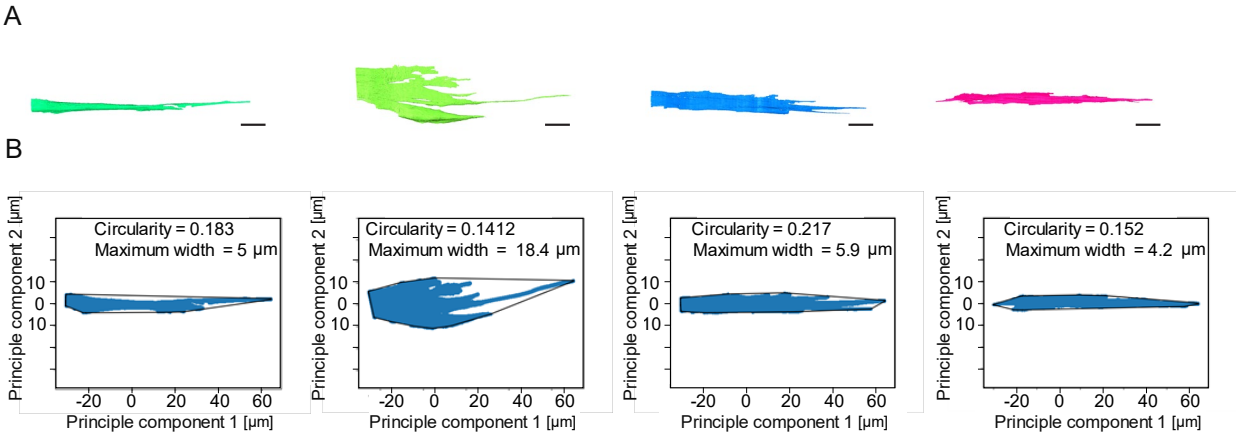

Figure S3. A) The analysis pipeline begins with the extraction of 3D segmented pericyte meshes. Shown here are four representative pericytes. B) Pericyte geometry is flattened into two principal dimensions using PCA by a Python-based image analysis pipeline. The 2D geometry's shape is then determined using convex hull analysis. To describe pericyte morphology, pericyte cell borders are analyzed for circularity, calculated as 4π*Area/Perimeter^2, where a value of 1 indicates a perfect circle and values approaching 0 indicate increasingly elongated shapes, and maximum width.

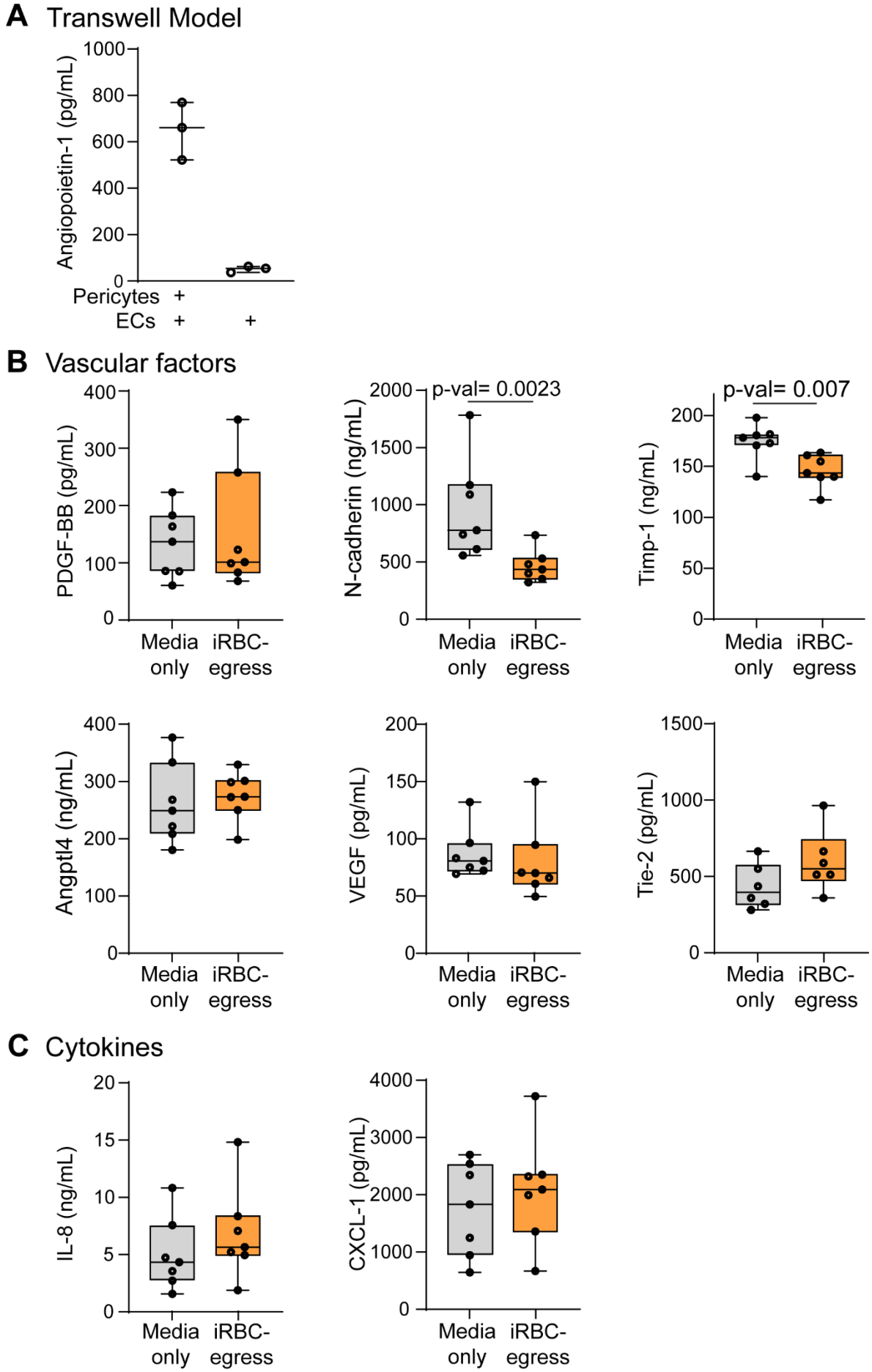
A Transwell Model
Angiopoietin-1 (pg/mL)
1000
800
600
400
200
0
Pericytes +
ECs + +
B Vascular factors
PDGF-BB (pg/mL)
N-cadherin (ng/mL)
p-val= 0.0023
Timp-1 (ng/mL)
p-val= 0.007
Angptl4 (ng/mL)
VEGF (pg/mL)
Tie-2 (pg/mL)
Media only
iRBC-egress
C Cytokines
IL-8 (ng/mL)
CXCL-1 (pg/mL)

878

Figure S4. A) Concentration of secreted angiopoietin-1 in supernatant obtained from either HBVP-HBMEC co-culture or HBMEC-only monolayers grown in a transwell model. Data points represent 3 independent experiments. Box and whisker plots display the median and the minimum and maximum data points. B) Concentrations of vascular factors PDGF-BB, N-cadherin, Timp-1, Angptl4, VEGF and Tie-2 measured by Luminex from 3D brain microvessels supernatants treated with media only or iRBC-egress media for 18-hours. C) Concentrations of released cytokines IL-8 and CXCL-1 measured by Luminex from 3D brain microvessels supernatants treated with media only or iRBC-egress media for 18-hours. Box and whisker plots display the median, 25th and 75th percentiles and the minimum and maximum data points in B and C. Data points represent supernatants pooled from 2-3 devices in 6-7 independent experiments. Statistical significance is analyzed by Mann-Whitney U test.

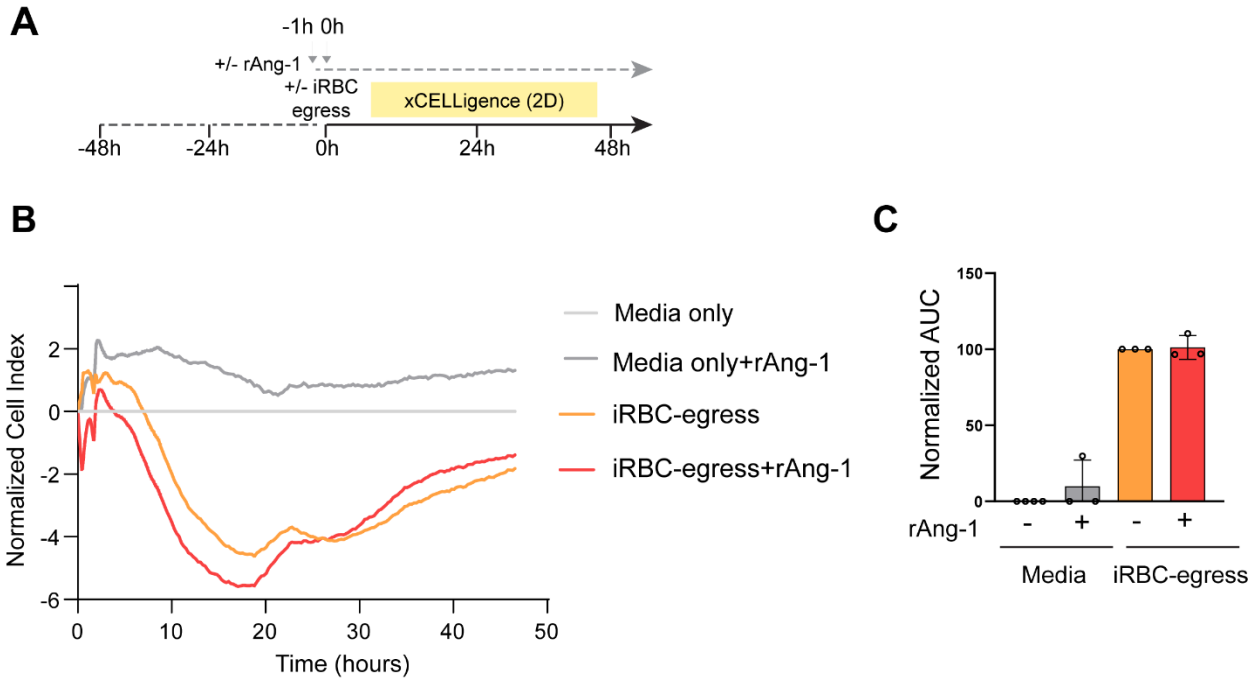

Figure S5. A) Experimental outline of short-term (1-hour) incubation with rAng-1 in a 2D HBMEC monolayer in the absence of HBVP. B) Representative recording data of xCELLigence measurements taken after +/- addition of rAng-1 followed by addition of media only or iRBC-egress media. All conditions were normalized to the media only control. C) Area under the curve analysis. All conditions were normalized to *P. falciparum*-iRBC-egress media as 100. Data points represent 3 independent experiments run in triplicate. Statistical significance is analyzed by repeated measures one-way ANOVA test with Dunnett's multiple comparisons test.